

Weak and Strong Constraint Data Assimilation in the inverse Regional Ocean Modeling System (ROMS): development and application for a baroclinic coastal upwelling system.

Emanuele Di Lorenzo^{a,*}, Andrew M. Moore^b, Hernan G. Arango^c, Bruce D. Cornuelle^d,
Arthur J. Miller^d, Brian Powell^b, Boon S. Chua^e, Andrew F. Bennett^e

^a*School of Earth and Atmospheric Sciences, Georgia Institute of Technology, Atlanta, Georgia*

^b*Department of Ocean Sciences, University of California, Santa Cruz, California*

^c*Institute of Marine and Coastal Sciences, Rutgers University, New Brunswick, New Jersey*

^d*Scripps Institution of Oceanography, University of California, San Diego, La Jolla, California*

^e*College of Oceanic and Atmospheric Sciences, Oregon State University, Corvallis, Oregon*

*Corresponding Author:

Emanuele Di Lorenzo

School of Earth and Atmospheric Sciences

Georgia Institute of Technology

311 Ferst Drive, Atlanta, GA 30332

Email: edl@gatech.edu

ABSTRACT

We describe the development and preliminary application of the inverse Regional Ocean Modeling System (ROMS), a four dimensional variational (4DVAR) data assimilation system for high-resolution basin-wide and coastal oceanic flows. Inverse ROMS makes use of the recently developed perturbation tangent linear (TL), representer tangent linear (RP) and adjoint (AD) models to implement an indirect representer-based generalized inverse modeling system. This modeling framework is modular. The TL, RP and AD models are used as stand-alone sub-models within the Inverse Ocean Modeling (IOM) system described in Chua and Bennett (2001). The system allows the assimilation of a wide range of observation types and uses an iterative algorithm to solve nonlinear assimilation problems. The assimilation is performed either under the perfect model assumption (strong constraint) or by also allowing for errors in the model dynamics (weak constraints). For the weak constraint case the TL and RP models are modified to include additional forcing terms on the right hand side of the model equations. These terms are needed to account for errors in the model dynamics.

Inverse ROMS is tested in a realistic 3D baroclinic upwelling system with complex bottom topography, characterized by strong mesoscale eddy variability. We assimilate synthetic data for upper ocean (0-450m) temperatures and currents over a period of 10 days using both a high resolution and a spatially and temporally aliased sampling array. During the assimilation period the flow field undergoes substantial changes from the initial state. This allows the inverse solution to extract the dynamically active information from the synthetic observations and improve the trajectory of the model state beyond the assimilation window. Both the strong and weak constraint assimilation experiments show forecast skill greater than persistence and climatology during the 10-20 days after the last observation is assimilated.

Further investigation in the functional form of the model error covariance and in the use of the representer tangent linear model may lead to improvement in the forecast skill.

Keywords: ROMS; Ocean models; Inverse methods; Tangent linear models; Adjoint models; Data assimilation;

1. Introduction

The regional ocean modeling system (ROMS) is a state-of-the-art free surface primitive equation ocean model capable of high resolution descriptions of coastal and basin-wide flows (Shchepetkin and McWilliams, 2005). The use of ROMS is widespread in the oceanographic community and a variety of studies exist that investigate the dynamics of ocean circulation in different regions of the world ocean (Haidvogel et al., 2000; Malanotte-Rizzoli et al., 2000; Miller et al., 2000; She and Klinck, 2000; Hermann et al., 2002; Di Lorenzo, 2003; Marchesiello et al., 2003; Robertson et al., 2003; Koster et al., 2004; Curchitser et al., 2005; Di Lorenzo et al., 2005; Kone et al., 2005; Miller et al., 2005; Penven et al., 2005; Warner et al., 2005).

Given the increasing number of oceanographic observations and ocean monitoring programs, there have been numerous developments of data assimilative frameworks that use advanced ocean models, such as ROMS. These systems are used to improve model representations of the ocean circulation at the global, basin-wide and regional scales, to test formal hypotheses in models by least squares and to assess observing systems. The assimilation schemes can be grouped into three main classes; (a) optimal interpolation, (b) sequential assimilation schemes based on Kalman Filtering and (c) four dimensional variational methods. A review of data assimilation methods and inverse theory used in oceanography, is available in Wunsch (1996), Bennett (1992; 2002), Anderson et al. (1996) and DeMey (1997), while a collection of oceanographic examples can be found in Malanotte-Rizzoli (1996) and Mooers (1999).

One important difference between four dimensional variational methods (4DVAR) and other assimilation schemes is that 4DVAR requires solving the adjoint equations of the dynamical system. This is usually done either through the use of an adjoint model or by direct computation of the adjoint matrix corresponding to the dynamical forward operator (the ocean model in this case). The adjoint equations describe the evolution of sensitivity to initial, boundary and parametric conditions backward in time (Courtier et al., 1993). These sensitivities contain important information, namely the Green's Function of the dynamical system, and can be used in an inverse framework to correct model initial and boundary conditions, model parameters, and model dynamics.

The adjoint method has been used for meteorological and oceanographic purposes in conjunction with a variety of models. For the ocean, these include simplified dynamic models, like the barotropic vorticity equation (Talagrand and Courtier, 1987; Gunson and MalanotteRizzoli, 1996; 1996) and shallow water models (Griffin and Thompson, 1996), quasi geostrophic models (Moore, 1991; Schroter et al., 1993; Seiler, 1993; Morrow and DeMey, 1995; Luong et al., 1998), residual mean circulation models (Ferreira et al., 2005), intermediate coupled ENSO prediction models (Kleeman et al., 1995; Galanti et al., 2003), and three

dimensional linear and nonlinear ocean models (Thepaut and Courtier, 1991; Tziperman et al., 1992; Tziperman et al., 1992; Lynch et al., 1998; Miller and Cornuelle, 1999; Cornuelle et al., 2000; Lynch and Hannah, 2001; Lynch and Naimie, 2002; Stammer et al., 2003; Di Lorenzo et al., 2004; Dommenges and Stammer, 2004; Stammer et al., 2004; Taillandier et al., 2004; He et al., 2005; Hoteit and Cornuelle, 2006; Lea et al., 2006) .

Earlier studies with a multilevel primitive-equation model (Thepaut and Courtier, 1991) demonstrate the efficiency of the 4DVAR approach in extracting the information contained in the dynamics of the model and in the observations. Other studies confirm that 4DVAR proves successful in reconstructing the unobserved part of the flow in the presence of baroclinic instability (Rabier and Courtier, 1992), a typical condition in the ocean. Although variational methods do not always perform well in the presence of strong nonlinearity, with strong non-Gaussian distribution of the errors (Miller et al., 1999), their success is confirmed by their wide use in Numerical Weather Prediction (NWP). 4DVAR-based schemes are routinely used at the European Center for Medium Range Weather Forecast (ECMWF) (Klinker et al., 2000; Mahfouf and Rabier, 2000), they have been developed for the US Naval Research Laboratory modeling framework (Rosmond and Xu, 2006) as well as for the National Center for Environmental Prediction (NCEP) model (Zou et al., 2001) and others (Zupanski et al., 2005).

In the oceanographic community, operational forecasting systems are based on optimal interpolation and sequential type methods. Examples of major systems include US NAVOCEANO forecasting system (Fox et al., 2002; Smedstad et al., 2003), the Hybrid Isopycnal Ocean Model (HYCOM) Nowcast/Forecast system (Chassignet et al., 2006), the Harvard Ocean Prediction System (HOPS) (Robinson and Walstad, 1987; Lermusiaux and Robinson, 1999; Robinson, 1999), the UK Met Office FOAM (Lorenç et al., 1991; Bell et al., 2000), the French MERCATOR system (De Mey and Benkiran, 2002), the Mediterranean Forecasting System (MFS) (Pinardi et al., 2003), and the Norwegian monitoring and predicting system TOPZ (Bertino and Lisaeter, 2006). Therefore the development of 4DVAR implementations for ocean models such as the OPA ocean model (Vialard et al., 2003; Weaver et al., 2003), the MIT general circulation model (Marshall et al., 1997; Marotzke et al., 1999) and ROMS (this paper), will enable the transition of ocean operational systems to 4DVAR.

In the 4DVAR applications mentioned so far, there is an implicit assumption that the model dynamics are perfect (strong constraint), which implies that the only control parameters to improve the fit of the model to the observations are the initial and boundary conditions, and model parameters. This assumption has been recently relaxed in the context of variational assimilation by the introduction of the direct representer method (Bennett and Thorburn, 1992). This method assumes that the model dynamics are not perfect (weak constraint) and

allows for corrections to the model dynamics. This is achieved by including a forcing term on the right hand side of the dynamical equations as additional control parameters of the inverse. Because the direct representer method is computationally expensive, later studies introduced a more efficient iterative approach referred to as the indirect representer method (Egbert et al., 1994) or four dimensional Physical-space Statistical Analysis System (Courtier, 1997).

The representer method has great potentials for assimilation of data into nonlinear models (Evensen, 1994) and comparisons done against sequential methods show that it can be more accurate (Ngodock et al., 2000; Kurapov et al., 2002). Data assimilation applications of the representer method, with the weak constraint formulations, have been used to study the tropical ocean circulation with a simple coupled ocean-atmosphere model (Bennett et al., 1998; 2000) and a reduced gravity primitive equation model (Ngodock, Chua, and Bennett, 2000; Bennett et al., 2006). Rosmond and Xu (2006) have used the representer based inversion to add 4DVAR capabilities to the US Navy's operational 3DVAR data assimilation system. The method has also been applied to improve estimates of global and coastal tides (Egbert, Bennett, and Foreman, 1994; Egbert and Erofeeva, 2002; Kurapov et al., 2003; Foreman et al., 2004). For coastal ocean applications, the representer method has been used to assimilate coastal currents in idealized linear model (Scott et al., 2000) and in a shallow water channel flow (Kurapov and Di Lorenzo, 2006). A comparison to other assimilation methods using a coastal baroclinic linear model is found in Kurapov et al. (2002). Other studies focused on more theoretical aspects of this method (Eknes and Evensen, 1997; Lyard, 1999; Uboldi and Kamachi, 2000) using 1D and 2D dynamical models.

This paper discusses the first implementation and application of the indirect representer method in ROMS, a fully nonlinear, state-of-the-art, primitive equation ocean model. Building on the recent development of the perturbation tangent linear (TL), representer tangent linear (RP) and adjoint (AD) models of ROMS (Moore et al., 2004), the implementation is achieved by interfacing the ROMS submodels with the Inverse Ocean modeling (IOM) system (Chua and Bennett, 2001). A similar implementation of IOM using a barotropic shallow water formulation of the spectral element ocean model (SEOM) is reported in Levin et al. (2006). The ROMS implementation may have direct impacts on existing ROMS-based forecasting systems (Wilkin et al., 2005) and on a variety of regional ocean applications where abundant observations are available.

Section 2 introduces the model and notation, section 3 present a derivation of the representer method in both the strong and weak constraint formulation. It also shows the theoretical equivalence between observation space inversions (e.g. representer method) with state space inversions (e.g. most 4DVAR frameworks). Section 4 derives the formulation of the right hand side forcing term in ROMS, which enable the weak constraint formulation. Section

5 presents the results and comparisons of the strong and weak constraint assimilation for a baroclinic coastal upwelling system. Section 6 presents a summary.

2. The models

Following the notation of Moore et al. (2004) we represent the nonlinear equations of NL-ROMS symbolically as:

$$\frac{\partial \mathbf{u}}{\partial t} = N(\mathbf{u}) + \mathbf{F}(t) \quad (2.1)$$

where $\mathbf{u}(t)$ denotes the model ocean state vector comprised of the prognostic variables at ocean grid points, $\mathbf{F}(t)$ is the right hand side forcing term, and $N(\mathbf{u})$ represents the model nonlinear dynamical operator. The dimension of the state vector will depend on the grid size and resolution of the model. If we linearize the model around a basic state $\mathbf{u}_B(t)$, then the evolution of $\mathbf{u}(t)$ is given by the tangent linearization of the nonlinear model, which we will also refer to as the representer tangent linear model (RP-ROMS):

$$\frac{\partial \mathbf{u}}{\partial t} = N(\mathbf{u}_B) + \left. \frac{\partial N}{\partial \mathbf{u}} \right|_{\mathbf{u}_B} (\mathbf{u} - \mathbf{u}_B) + \mathbf{F}(t) \quad (2.2)$$

where $\mathbf{s} = \mathbf{u} - \mathbf{u}_B$ are small perturbations around the basic state. The dynamical evolution $\mathbf{s}(t)$ is given by the perturbation tangent linear model (TL-ROMS):

$$\frac{\partial \mathbf{s}}{\partial t} = \left. \frac{\partial N}{\partial \mathbf{u}} \right|_{\mathbf{u}_B} \mathbf{s} = \mathbf{A} \mathbf{s} \quad (2.3)$$

where the matrix operator $\mathbf{A} \equiv \left. \frac{\partial N}{\partial \mathbf{u}} \right|_{\mathbf{u}_B}$. The adjoint model (AD-ROMS) of (2.3) is derived from the perturbation tangent linear model using the L2-norm, and is represented by:

$$-\frac{\partial \lambda}{\partial t} = \mathbf{A}^T \lambda \quad (2.4)$$

In the indirect representer-based inverse method, described in the next section, it is assumed that the model dynamics, boundary conditions and the initial conditions are all uncertain. If we assume that the errors are small, their dynamics are described by the linear models RP-ROMS (2.2) and TL-ROMS (2.3)

$$\frac{\partial \mathbf{u}}{\partial t} = N(\mathbf{u}_B) + \left. \frac{\partial N}{\partial \mathbf{u}_B} \right|_{\mathbf{u}_B} (\mathbf{u} - \mathbf{u}_B) + \mathbf{F}(t) + \mathbf{e}(t) \quad (2.5)$$

$$\frac{\partial \mathbf{s}}{\partial t} = \mathbf{A}\mathbf{s} + \mathbf{e}(t) \quad (2.6)$$

where the forcing term $\mathbf{e}(t)$ on the right hand side explicitly accounts for missing model dynamics, and errors in the forcing, boundary conditions and initial conditions. Note that in the TL equations (2.3) and (2.6), the forcing terms $\mathbf{f}(t)$ and $\mathbf{e}(t)$ are formally the same. The corresponding integral solution of (2.1), (2.5), (2.6) and (2.4) will be denoted respectively as:

$$\mathbf{u}(t_N) = \mathbf{N}[\mathbf{u}(t_0), t_0, t_N] \quad (2.7)$$

$$\mathbf{u}(t_N) = \mathbf{R}(t_0, t_N)\mathbf{u}(t_0) + \int_{t_0}^{t_N} \mathbf{R}(t', t_N)[N(\mathbf{u}_B) + \mathbf{F}(t') + \mathbf{e}(t')]dt' \quad (2.8)$$

$$\mathbf{s}(t_N) = \mathbf{R}(t_0, t_N)\mathbf{s}(t_0) + \int_{t_0}^{t_N} \mathbf{R}(t', t_N)\mathbf{e}(t')dt' \quad (2.9)$$

$$\lambda(t_0) = \mathbf{R}^T(t_N, t_0)\lambda(t_N) \quad (2.10)$$

where \mathbf{N} is the nonlinear forward operator and $\mathbf{R}(t_0, t_N)$ is the tangent linear propagator for the interval $[t_0, t_N]$. We refer to (2.8) as the RP-ROMS and (2.9) as TL-ROMS. The corresponding adjoint propagator $\mathbf{R}^T(t_N, t_0)$ is defined for the interval $[t_N, t_0]$ and is often referred to as the backward integration because it propagates the model state backward in time. The first-term on the right hand side of (2.8) and (2.9) propagates the initial condition forward in time according to the tangent model dynamics. The integral on the right hand side involving $\mathbf{e}(t')$ indicates that corrections to the model dynamics, boundary conditions, and initial condition are introduced at each time as a forcing impulse $\mathbf{e}(t')$ and are independently propagated forward from time t' when they are introduced to the final time t_N . Using this convention, the corrections in the initial conditions are represented as a forcing impulse $\mathbf{e}(t) = \mathbf{e}_0\delta(t_0 - t)$ at the initial time.

In the implementation of inverse ROMS the adjoint model can also be forced on the right hand side by any impulse $\widehat{\mathbf{e}}(t)$, and the corresponding integral solution becomes:

$$\boldsymbol{\lambda}(t_0) = \mathbf{R}^T(t_N, t_0)\boldsymbol{\lambda}(t_N) + \int_{t_0}^{t_N} \mathbf{R}^T(t', t_0)\hat{\mathbf{e}}(t)dt'. \quad (2.11)$$

A detailed description of the development and implementation of TL-ROMS and AD-ROMS is found in Moore et al. (2004). RP-ROMS is introduced here for the first time, however its structure is exactly as TL-ROMS except that the basic state terms are retained. A derivation of the full equations in continuous form is also available from Arango et al. (2006). The RP-ROMS and TL-ROMS have been modified from their original implementation to account for the additional terms on the right hand side of the models equations. These developments are described in section 4.

3. Assimilation method and implementation of inverse ROMS

We describe next the indirect representer method (hereinafter referenced as IRM) used to assimilate ocean observations in inverse ROMS. From now on we will refer to IRM as the representer based 4DVAR, in which the inverse solution is found in observation space, while we will retain the phrase 4DVAR for the state space inversions. The derivation will use matrix vector notation and solutions are expressed in integral form to maintain a closer correspondence to the model source codes, which are written in discrete form. This notation also allows us to show how ocean estimates obtained by IRM are analogous to the state space inversions of 4DVAR methods described by Courtier (1997). Derivations that make use of the continuous form can be found in Bennett (1992; 2002) and Chua and Bennett (2001).

The goal of the IRM and 4DVAR is to produce the best estimate, in a least square sense, of the model state $\hat{\mathbf{u}}(t)$ that agrees with available ocean observations within measurement error

$$\boldsymbol{\varepsilon} = \mathbf{d} - L[\hat{\mathbf{u}}(t)] \quad (3.1)$$

where \mathbf{d} is an array of observations at different temporal and spatial locations, $L[]$ is a sampling/measurement functional which maps the model state vector into observation space, and $\boldsymbol{\varepsilon}$ is the misfit between model and data, which ideally should be smaller or equal to measurement error once the best estimate $\hat{\mathbf{u}}$ is found. $L[]$ can be a nonlinear function, however for simplicity and to facilitate the following development we assume that $L[]$ is linear over the period when observations are available $[t_0, T]$, and defined as:

$$L[\hat{\mathbf{u}}] = \int_{t_0}^T \mathbf{H}(t') \hat{\mathbf{u}}(t') dt' . \quad (3.2)$$

In both the IRM and 4DVAR method, a “prior estimate” of the model ocean state $\mathbf{u}_F^n(t)$ is corrected using an iterative approach, so that:

$$\hat{\mathbf{u}}^n(t) = \mathbf{u}_F^n(t) + \mathbf{s}^n(t) \quad (3.3)$$

where for each iteration, n , the small corrections $\mathbf{s}^n(t)$ are sought and applied to the prior model trajectory $\mathbf{u}_F^n(t)$ to produce a new estimate $\hat{\mathbf{u}}^n(t)$. The corrections $\mathbf{s}^n(t)$ during the first iteration are computed by exploring the linear sensitivity of the ocean model using the TL and AD models linearized around the basic state $\mathbf{u}_B(t)$. During subsequent iterations the new estimate $\hat{\mathbf{u}}^n(t)$ provides the linearization basic state for TL and AD. The iteration is repeated until the estimated state $\hat{\mathbf{u}}^n(t)$ agrees with the observations within some specified tolerance.

Let us denote by $\hat{\mathbf{d}} = \mathbf{d} - L[\mathbf{u}_F^n(t)]$ the model-observation misfit for the initial guess. Substituting (3.3) into (3.1) and applying the definition for $L[\]$ in (3.2) yields:

$$\boldsymbol{\varepsilon} = \hat{\mathbf{d}} - \int_{t_0}^T \mathbf{H}(t') \mathbf{s}^n(t') dt' \quad (3.4)$$

$$\mathbf{s}^n(t') = \int_{t_0}^{t'} \mathbf{R}(t'', t') \mathbf{e}(t'') dt'' \quad (3.5)$$

where (3.5) is the perturbation tangent linear model (2.9), which controls the dynamical evolution of small corrections $\mathbf{s}^n(t)$ about the basic state $\hat{\mathbf{u}}^n(t)$. The trajectory of $\mathbf{s}^n(t)$ depends on corrections $\mathbf{e}(t)$ in the model dynamics, boundary conditions and initial conditions. The first term of (2.9) involving the initial condition $\mathbf{s}^n(t_0)$ has been omitted because corrections at the initial time are applied as impulse $\mathbf{e}(t) = \mathbf{e}_0 \delta(t_0 - t)$.

During each iteration n we seek to minimize $\boldsymbol{\varepsilon}$ in a least square sense by minimizing a quadratic penalty (or cost) function given by:

$$J[\mathbf{e}] = \boldsymbol{\varepsilon}^T \mathbf{C}_{\boldsymbol{\varepsilon}}^{-1} \boldsymbol{\varepsilon} + \int_{t_0}^T \int_{t_0}^T \mathbf{e}^T(t') \mathbf{C}^{-1}(t', t'') \mathbf{e}(t'') dt' dt'' \quad (3.6)$$

where $\boldsymbol{\varepsilon} = \hat{\mathbf{d}} - \int_{t_0}^T \mathbf{H}(t') \int_{t_0}^{t'} \mathbf{R}(t'', t') \mathbf{e}(t'') dt'' dt'$ from (3.4) and (3.5). The first term of (3.6) is the penalty associated with the model minus observation misfit, and the covariance $\mathbf{C}_{\boldsymbol{\varepsilon}} = \overline{\boldsymbol{\varepsilon} \boldsymbol{\varepsilon}^T}$ indicates that the corrections $\mathbf{e}(t)$ should reduce the model minus observation misfit to within observational error. The second term ensures that as we seek the minimum of J , the corrections $\mathbf{e}(t)$ should not exceed our assumptions about the errors in the model dynamics, boundary conditions and initial condition. These assumptions are expressed in the covariance matrix $\mathbf{C}(t', t'') = \overline{\mathbf{e}(t') \mathbf{e}^T(t'')}$ used to weight $\mathbf{e}(t)$. An extremum of J is found by setting $\partial J / \partial \mathbf{e} = 0$ and solving for $\mathbf{e}(t)$. However it is important to recall that the solution $\mathbf{e}(t)$ that minimizes J is equivalent to finding the value of $\mathbf{e}(t)$ that maximizes the probability distribution of $\mathbf{e}(t)$ conditioned on the model-minus-observation misfit. This result follows from the choice of a quadratic J and the identity $-\ln[\text{Prob}(\mathbf{e} \mid \hat{\mathbf{d}})] = J[\mathbf{e}]$, and implies that $\mathbf{e}(t)$ is an optimal estimate only if the true probability distribution is Gaussian. A Gaussian distribution is not guaranteed for the error statistics of the initial conditions, model dynamics and boundary conditions. If the distribution is non-Gaussian the minimum of J will lead to a non optimal estimate of $\mathbf{e}(t)$ or, in the case of a heavily non-Gaussian distribution, to a very improbable estimate.

In the following subsections we proceed to find the $\mathbf{e}(t)$ that minimizes J and obtain an expression for the required correction $\mathbf{s}^n(t)$ to the model initial guess $\mathbf{u}_F^n(t)$.

3.1 The strong constraint case

We consider first the case in which the model dynamics and boundary conditions are assumed to be free of error. In this case changes in $\mathbf{e}(t)$ are allowed only at the initial time ($\mathbf{e}(t_0) = \mathbf{e}_0$) to account for errors in the model initial conditions. Combining (3.4) and (3.5), and using the definition $\mathbf{e}(t'') = \mathbf{e}_0 \delta(t_0 - t'')$, the expression for the model minus observation misfit simplifies to:

$$\boldsymbol{\varepsilon} = \hat{\mathbf{d}} - \int_{t_0}^T \mathbf{H}(t') \underbrace{\mathbf{R}(t_0, t') \mathbf{e}_0}_{\mathbf{s}^n(t')} dt' \quad (3.7)$$

where the second term on the right hand side represents the perturbation tangent linear model forced by a correction in the initial state \mathbf{e}_0 . The integral sign and the \mathbf{H} operator indicate that the tangent linear is sampled at the observation locations in space and time. Substitution of (3.7) into the penalty function (3.6) yields:

$$J[\mathbf{e}(t_0)] = \left[\hat{\mathbf{d}} - \int_{t_0}^T \mathbf{H}(t') \mathbf{R}(t_0, t') dt' \mathbf{e}_0 \right]^T \mathbf{C}_\varepsilon^{-1} \left[\hat{\mathbf{d}} - \int_{t_0}^T \mathbf{H}(t') \mathbf{R}(t_0, t') dt' \mathbf{e}_0 \right] + \mathbf{e}_0^T \mathbf{P}^{-1} \mathbf{e}_0 \quad (3.8)$$

where $\mathbf{P} \equiv \mathbf{C}(t_0, t_0)$ is the covariance of the error in initial conditions, and we have made use of the definition $\mathbf{e}(t'') = \mathbf{e}_0 \delta(t_0 - t'')$. To find the minimum of J we set $\partial J / \partial \mathbf{e} = 0$ so that:

$$\frac{\partial J[\mathbf{e}_0]}{\partial \mathbf{e}_0} = 2 \left[- \int_{t_0}^T \mathbf{H}(t') \mathbf{R}(t_0, t') dt' \right]^T \mathbf{C}_\varepsilon^{-1} \left[\hat{\mathbf{d}} - \int_{t_0}^T \mathbf{H}(t') \mathbf{R}(t_0, t') dt' \mathbf{e}_0 \right] + 2 \mathbf{P}^{-1} \mathbf{e}_0 = 0 \quad (3.9)$$

After regrouping (3.9) we obtain the following linear system of equations:

$$\underbrace{\left(\int_{t_0}^T \mathbf{R}^T(t', t_0) \mathbf{H}^T(t') dt' \mathbf{C}_\varepsilon^{-1} \int_{t_0}^T \mathbf{H}(t') \mathbf{R}(t_0, t') dt' + \mathbf{P}^{-1} \right)}_{\hat{\mathbf{H}}} \mathbf{e}_0 = \int_{t_0}^T \mathbf{R}^T(t', t_0) \mathbf{H}^T(t') dt' \mathbf{C}_\varepsilon^{-1} \hat{\mathbf{d}}. \quad (3.10)$$

The system (3.10) can be rewritten using the matrix identity $(\mathbf{G}^T \mathbf{C}_\varepsilon^{-1} \mathbf{G} + \mathbf{P}^{-1})^{-1} \mathbf{G}^T \mathbf{C}_\varepsilon^{-1} = (\mathbf{P} \mathbf{G}^T) (\mathbf{G} \mathbf{P} \mathbf{G}^T + \mathbf{C}_\varepsilon)^{-1}$ with $\mathbf{G} \equiv \int_{t_0}^T \mathbf{H}(t') \mathbf{R}(t_0, t') dt'$, This identity, which is a variant of the matrix inversion lemma (see Haykin, 1996), yields:

$$\underbrace{\left(\int_{t_0}^T \mathbf{H}(t') \mathbf{R}(t_0, t') dt' \mathbf{P} \int_{t_0}^T \mathbf{R}^T(t', t_0) \mathbf{H}^T(t') dt' + \mathbf{C}_\varepsilon \right)}_{\hat{\mathbf{P}}} \underbrace{\left(\mathbf{P} \int_{t_0}^T \mathbf{R}^T(t', t_0) \mathbf{H}^T(t') dt' \right)^{-1}}_{\beta^n} \mathbf{e}_0 = \hat{\mathbf{d}}. \quad (3.11)$$

The state space 4DVAR implementations seek solutions of (3.10) that require estimates of the inverse of the matrix $\hat{\mathbf{H}}$, referred as to the Hessian ($\partial^2 J / \partial \mathbf{e}_0^2 = \hat{\mathbf{H}}$) or Fisher matrix. Although $\hat{\mathbf{H}}$ is symmetric and positive definite, a direct inversion is prohibitive because the dimensions are of the size of the state and therefore large. Typically in 4DVAR different strategies are used to evaluate \mathbf{e}_0 by computing the direct action of $\hat{\mathbf{H}}$ on different guesses of the vector \mathbf{e}_0 , without ever solving the system iteratively. Once \mathbf{e}_0 is found, the ocean state new estimate is:

$$\hat{\mathbf{u}}^n(t) = \mathbf{u}_F^n(t) + \mathbf{s}^n(t) = \mathbf{u}_F^n(t) + \mathbf{R}(t_0, t) \mathbf{e}_0. \quad (3.12)$$

The actual evaluation of the new trajectory $\hat{\mathbf{u}}^n(t)$ is done by correcting the initial condition of the nonlinear model $\hat{\mathbf{u}}^n(t_0) = \hat{\mathbf{u}}_F^n(t_0) + \mathbf{e}_0$. The nonlinear model is then integrated forward to generate the estimate $\hat{\mathbf{u}}^n(t)$. This new estimate should be close to the one obtained by (3.12) if the dynamics of the nonlinear model behave linearly over the assimilation period $[t_0, T]$. The new trajectory of the nonlinear model is then sampled at observation locations to reevaluate the model minus observation misfit $\hat{\mathbf{d}} = \mathbf{d} - L[\mathbf{u}_F^n(t)]$ and the cost function J . If the new estimate is not satisfactory, the nonlinear model trajectory becomes the new initial guess for the next iteration $\mathbf{u}_F^{n+1}(t) = \hat{\mathbf{u}}^n(t)$ and the iterative procedure continues until a minimum is found.

The IRM implementation of inverse ROMS, uses an alternative method to estimate \mathbf{e}_0 by solving the system (3.11). Although this approach is different from 4DVAR, which solves (3.10),

the two systems lead to the same estimate of \mathbf{e}_0 . In IRM the matrix $\hat{\mathbf{P}}$, which is referred as the stabilized representer matrix, has dimensions of (observations x observations), and represents a data error covariance matrix conditioned on the model initial condition uncertainties. Similar to the state space 4DVAR approach, the action of $\hat{\mathbf{P}}$ on a vector is evaluated in order to find the vector $\boldsymbol{\beta}^n$, which is referred to as the representer coefficients vector for iteration n (a description of the method of solution in inverse ROMS is provided in section 3.3). Once $\boldsymbol{\beta}^n$ is found, we compute the initial condition corrections \mathbf{e}_0 through the identity $\mathbf{e}_0 \equiv \mathbf{P} \int_0^T \mathbf{R}^T(t', t_0) \mathbf{H}^T(t') dt' \boldsymbol{\beta}^n$, which follows from (3.11). This identity shows that the corrections \mathbf{e}_0 can be obtained by forcing the adjoint model \mathbf{R}^T at the observation locations with impulses given by the representer coefficients vector $\boldsymbol{\beta}^n$. \mathbf{H}^T is the adjoint operator of the sampling function \mathbf{H} , and provides the mapping from observation to model space. Substituting \mathbf{e}_0 in (3.12) the update of the ocean estimate becomes:

$$\hat{\mathbf{u}}^n(t) = \mathbf{u}_F^n(t) + \mathbf{s}^n(t) = \mathbf{u}_F^n(t) + \mathbf{R}(t_0, t) \underbrace{\mathbf{P} \int_{t_0}^T \mathbf{R}^T(t', t_0) \mathbf{H}^T(t') dt'}_{\mathbf{e}_0} \boldsymbol{\beta}^n \quad (3.13)$$

This method of solution is also referred to as the representer method (Bennett, 1992) and as PSAS (Courtier, 1997). If we define the symmetric covariance matrix

$$\widehat{\mathbf{R}}(t', t'') \equiv \mathbf{R}(t_0, t') \mathbf{P} \mathbf{R}^T(t'', t_0) \quad (3.14)$$

as the full representer matrix in model space (also referred to as the *reproducing kernel*) the system (3.11) becomes

$$\underbrace{\left(\int_{t_0}^T \int_{t_0}^T \mathbf{H}(t') \widehat{\mathbf{R}}(t', t'') \mathbf{H}^T(t'') dt'' dt' + \mathbf{C}_\varepsilon \right)}_{\hat{\mathbf{P}}} \underbrace{\left(\mathbf{P} \int_{t_0}^T \mathbf{R}^T(t', t_0) \mathbf{H}^T(t') dt' \right)^{-1}}_{\boldsymbol{\beta}^n} \mathbf{e}_0 = \hat{\mathbf{d}}. \quad (3.15)$$

The update of the state can be expressed also as a function of the representer matrix and coefficients as:

$$\hat{\mathbf{u}}^n(t) = \mathbf{u}_F^n(t) + \mathbf{s}^n(t) = \mathbf{u}_F^n(t) + \int_{t_0}^T \widehat{\mathbf{R}}(t, t'') \mathbf{H}^T(t'') dt'' \boldsymbol{\beta}^n. \quad (3.16)$$

In the strong constraint case, the *reproducing kernel* matrix has the physical meaning of projecting the initial uncertainty covariance \mathbf{P} into a covariance in full model state space, where each column of $\widehat{\mathbf{R}}$ corresponds to the covariance of a model grid point at a particular time with all other grid points at all times. The update to the state is then obtained by projecting the vector $\boldsymbol{\beta}^n$ onto the (state space x observation space) covariance in (3.16). The *reproducing kernel* is computed using the tangent and adjoint models \mathbf{R} and \mathbf{R}^T according to (3.14).

Before providing a detail description of how IRM is implemented for inverse ROMS we proceed to derive the form of the solution for the more general weak constraint assimilation case.

3.2 The weak constraint case

We now consider the general case in which the model dynamics, boundary conditions and initial conditions need to be corrected. After combining (3.4) and (3.5), the expression for the model-observation misfit is:

$$\boldsymbol{\varepsilon} = \hat{\mathbf{d}} - \int_{t_0}^T \mathbf{H}(t') \underbrace{\int_{t_0}^{t'} \mathbf{R}(t'', t') \mathbf{e}(t'') dt''}_{\mathbf{s}^n(t')} dt' = \int_{t_0}^T \underbrace{\int_{t''}^T \mathbf{H}(t') \mathbf{R}(t'', t') dt'}_{\mathbf{G}(t'')} \mathbf{e}(t'') dt'' \quad (3.17)$$

where the operator $\mathbf{G}(t'')$ is defined as:

$$\mathbf{G}(t'') \equiv \int_{t''}^T \mathbf{H}(t') \mathbf{R}(t'', t') dt'. \quad (3.18)$$

The model misfit simplifies to:

$$\boldsymbol{\varepsilon} = \hat{\mathbf{d}} - \int_{t_0}^T \mathbf{G}(t'') \mathbf{e}(t'') dt'' \quad (3.19)$$

Physically \mathbf{G} maps the action of the tangent model dynamics \mathbf{R} from model space to observation space for any given time t'' . Therefore the action of \mathbf{G} on $\mathbf{e}(t)$ over the time

integral $[t_0, T]$ corresponds to integrating the tangent model forward forced by the correction $\mathbf{e}(t)$ and sampling the solution at observation locations.

Substituting $\boldsymbol{\varepsilon}$ from (3.19) in the penalty function (3.6), and equating $\partial J / \partial \mathbf{e} = 0$ yields:

$$\int_{t_0}^T \underbrace{[\mathbf{G}^T(t)\mathbf{C}_\varepsilon^{-1}\mathbf{G}(t') + \mathbf{C}^{-1}(t, t')]_{\hat{\mathbf{H}}(t, t')}} \mathbf{e}(t') dt' = \mathbf{G}^T(t)\mathbf{C}_\varepsilon^{-1}\hat{\mathbf{d}}. \quad (3.20)$$

Here the Hessian matrix $\hat{\mathbf{H}}$ is extremely large when compared to the strong constraint case (3.10). Solving the system (3.20) involves computing the action of $\hat{\mathbf{H}}$ on a vector for all times $[t_0, T]$. Given that the dimension of $\hat{\mathbf{H}}$ are already very large for typical applications of realistic ocean models (state space x state space), solving (3.20) for each time may be computationally prohibitive. However, in the strong constraint case, we can rewrite the system (3.20) using the matrix inversion lemma to obtain the system:

$$\underbrace{\int_{t_0}^T \int_{t_0}^T [\mathbf{G}(t')\mathbf{C}(t', t'')\mathbf{G}^T(t'') + \mathbf{C}_\varepsilon] dt' dt''}_{\hat{\mathbf{P}}} \underbrace{\int_{t_0}^T \int_{t_0}^T [\mathbf{C}(t', t'')\mathbf{G}^T(t'')]^{-1} \mathbf{e}(t') dt' dt''}_{\boldsymbol{\beta}^n} = \hat{\mathbf{d}} \quad (3.21)$$

The system (3.21) is the equivalent of the strong constraint case (3.11) with a time convolution added. The IRM implementation for inverse ROMS solves (3.21). One advantage of solving the system (3.21) is that the dimensions of $\hat{\mathbf{P}}$ are still in observation space, and have not changed from the strong constraint case. As shown in the next section, the action of $\hat{\mathbf{P}}$ on $\boldsymbol{\beta}^n$ can be evaluated by an integration of the adjoint model forced at observation locations (\mathbf{G}^T) followed by a forward integration of the tangent model forced with the convolved adjoint solution through $\mathbf{C}(t', t'')$ and sampled at observation locations by \mathbf{G} . In this way (3.21) can be solved iteratively. Once $\boldsymbol{\beta}^n$ has been computed, the corrections $\mathbf{e}(t)$ are evaluated using the definition in (3.21):

$$\mathbf{e}(t) = \int_{t_0}^t \mathbf{C}(t, t'')\mathbf{G}^T(t'')\boldsymbol{\beta}^n dt''. \quad (3.22)$$

Substituting the definition of $\mathbf{G}(t'') \equiv \int_{t''}^T \mathbf{H}(t')\mathbf{R}(t'', t') dt'$ back into (3.21) and (3.22) yields:

$$\underbrace{\left[\int_0^T \int_0^T \int_{t'}^T \mathbf{H}(\hat{t}) \mathbf{R}(t', \hat{t}) d\hat{t} \mathbf{C}(t', t'') \int_{t''}^T \mathbf{R}^T(\hat{t}, t'') \mathbf{H}^T(\hat{t}) d\hat{t} dt' dt'' + \mathbf{C}_s \right]}_{\hat{\mathbf{P}}} \boldsymbol{\beta}^n = \hat{\mathbf{d}} \quad (3.23)$$

and

$$\mathbf{e}(t) = \int_{t_0}^t \mathbf{C}(t, t'') \int_{t''}^T \mathbf{R}^T(t', t'') \mathbf{H}^T(t') dt' \boldsymbol{\beta}^n dt'' \quad (3.24)$$

Finally the update to the ocean model state is

$$\hat{\mathbf{u}}^n(t) = \mathbf{u}_F^n(t) + \mathbf{s}^n(t) = \mathbf{u}_F^n(t) + \int_{t_0}^t \mathbf{R}(t', t) \mathbf{e}(t') dt' \quad (3.25)$$

As in the strong constraint case, we define the full representer matrix

$$\widehat{\mathbf{R}}(\hat{t}, \hat{t}) \equiv \int_{t_0}^{\hat{t}} \int_{t_0}^{\hat{t}} \mathbf{R}(t', \hat{t}) \mathbf{C}(t', t'') \mathbf{R}^T(\hat{t}, t'') dt'' dt' \quad (3.26)$$

and note that the integrals on left-hand side of (3.23) can be rearranged so that:

$$\begin{aligned} \int_0^T \int_0^T \int_{t'}^T \mathbf{H}(\hat{t}) \mathbf{R}(t', \hat{t}) d\hat{t} \mathbf{C}(t', t'') \int_{t''}^T \mathbf{R}^T(\hat{t}, t'') \mathbf{H}^T(\hat{t}) d\hat{t} dt' dt'' &= \\ = \int_0^T \mathbf{H}(\hat{t}) \int_0^T \int_{t_0}^{\hat{t}} \int_{t_0}^{\hat{t}} \mathbf{R}(t', \hat{t}) \mathbf{C}(t', t'') \mathbf{R}^T(\hat{t}, t'') dt'' dt' \mathbf{H}^T(\hat{t}) d\hat{t} & \end{aligned} \quad (3.27)$$

The system (3.21) can be rewritten as a function of the full representer matrix:

$$\underbrace{\left[\int_0^T \mathbf{H}(\hat{t}) \int_0^T \widehat{\mathbf{R}}(\hat{t}, \hat{t}) \mathbf{H}^T(\hat{t}) d\hat{t} d\hat{t} + \mathbf{C}_s \right]}_{\hat{\mathbf{P}}} \boldsymbol{\beta}^n = \hat{\mathbf{d}} \quad (3.28)$$

and the corrections to the ocean model state are given by:

$$\hat{\mathbf{u}}^n(t) = \mathbf{u}_F^n(t) + \mathbf{s}^n(t) = \mathbf{u}_F^n(t) + \int_{t_0}^t \widehat{\mathbf{R}}(t, t'') \mathbf{H}^T(t'') dt'' \boldsymbol{\beta}^n \quad (3.29)$$

This is the form of the solution obtained via alternative derivations using the nonlinear Euler-Lagrange equations (Chua and Bennett, 2001; Bennett, 2002)

3.3 The inverse ROMS implementation and method of solution

The IRM implementation of inverse ROMS solves the system (3.23) using the IOM framework (Chua and Bennett, 2001). We next describe below the method of solution for (3.23), and how the NL-ROMS, RP-ROMS, TL-ROMS and AD-ROMS are integrated within the IOM. The first step is to compute the model basic state $\mathbf{u}_B(t)$ using the nonlinear model NL-ROMS over the assimilation time interval $[t_0, T]$, initialized with initial condition $\hat{\mathbf{u}}_0$

$$\mathbf{u}_B(t) = \mathbf{N}[\hat{\mathbf{u}}_0, \mathbf{F}(t), t_0, t] \quad (3.30)$$

We next compute the ‘‘first guess’’ estimate of the ocean state $\mathbf{u}_F^n(t)$ using the representer tangent linear model RP-ROMS, for $n = 0$

$$\mathbf{u}_F^n(t) = \mathbf{R}(t_0, t)\hat{\mathbf{u}}_0 + \int_{t_0}^t \mathbf{R}(t', t)[N(\mathbf{u}_B) + \mathbf{F}(t')]dt' \quad (3.31)$$

During the first iteration ($n = 0$), NL-ROMS solution is used as the basic state around which the dynamics are linearized. The model-minus-observations misfit $\hat{\mathbf{d}}^n$ during the first iteration is obtained by sampling the model state through the measurement function $L[\mathbf{u}_F^n]$

$$\hat{\mathbf{d}}^n = \mathbf{d} - \int_{t_0}^T \mathbf{H}(t')\mathbf{u}_F^n(t)dt' \quad (3.32)$$

We next solve the system $\hat{\mathbf{P}}\hat{\boldsymbol{\beta}}^n = \hat{\mathbf{d}}^n$ (3.23) to find the representer coefficients $\hat{\boldsymbol{\beta}}^n$. In IOM (3.23) is solved iteratively using the conjugate gradient algorithm (Golub and Van Loan, 1982), during which the action of the symmetric matrix $\hat{\mathbf{P}}$ on a vector $\boldsymbol{\psi}$ is evaluated. Rearranging the time integrals in (3.23) so that:

$$\hat{\mathbf{P}}\boldsymbol{\psi} = \int_{t_0}^T \mathbf{H}(\hat{t}) \underbrace{\int_{t_0}^{\hat{t}} \mathbf{R}(t', \hat{t}) \int_{t_0}^T \mathbf{C}(t', t'') \underbrace{\int_{t''}^T \mathbf{R}^T(\hat{t}, t'')\mathbf{H}^T(\hat{t})\boldsymbol{\psi}d\hat{t}}_{\boldsymbol{\lambda}(t'') \text{ Adjoint Solution}} dt'' dt'}_{\mathbf{f}(t') \text{ Convolution of Adjoint Solution}} dt' + \mathbf{C}_\varepsilon\boldsymbol{\psi} \quad (3.33)$$

$\underbrace{\hspace{15em}}_{\boldsymbol{\tau}(\hat{t}) \text{ Tangent Linear model forced with } \mathbf{f}(t')}$
 $\underbrace{\hspace{15em}}_{\text{Sampling of Tangent Linear solution } \boldsymbol{\tau}(\hat{t})}$

where each integral of (3.33) can be identified with one of the ROMS models. (3.33) is evaluated in the so-called “inner loop”, where the action of $\widehat{\mathbf{P}}$ (the stabilized representer matrix) is computed using the adjoint and perturbation tangent models as follows:

(i) integrate AD-ROMS forced with any vector $\boldsymbol{\psi}$ at the observation locations and generate the adjoint model trajectory $\boldsymbol{\lambda}(t'')$,

$$\boldsymbol{\lambda}(t'') = \int_{t''}^T \mathbf{R}^T(\hat{t}, t'') \mathbf{H}^T(\hat{t}) \boldsymbol{\psi} d\hat{t}; \quad (3.34)$$

(ii) convolve the adjoint solution with the model error covariance,

$$\mathbf{f}(t') = \int_{t_0}^T \mathbf{C}(t', t'') \boldsymbol{\lambda}(t'') dt''. \quad (3.35)$$

Note that the dimension of $\mathbf{C}(t', t'')$ are extremely large and a direct computation of the convolution in (3.35) may seem prohibitive. However, as will be described in section 5.4, for particular functional choices of $\mathbf{C}(t', t'')$ (e.g. Gaussian shape) this calculation is affordable, although still expensive.

(iii) force the tangent model TL-ROMS with $\mathbf{f}(t')$,

$$\boldsymbol{\tau}(\hat{t}) = \int_{t_0}^{\hat{t}} \mathbf{R}(t', \hat{t}) \mathbf{f}(t') dt'; \quad (3.36)$$

and (iv) evaluate the action of $\widehat{\mathbf{P}}$ on the vector $\boldsymbol{\psi}$ by sampling the tangent model trajectory $\boldsymbol{\tau}(\hat{t})$ and adding the data error covariance term

$$\widehat{\mathbf{P}}\boldsymbol{\psi} \equiv \int_{t_0}^T \mathbf{H}(\hat{t}) \boldsymbol{\tau}(\hat{t}) d\hat{t} + \mathbf{C}_\varepsilon \boldsymbol{\psi}. \quad (3.37)$$

Once the inner loop has converged we obtain an estimate of $\boldsymbol{\beta}^n$. The number of inner loop iterations is smaller than or equal to the total number of observations. We then integrate the adjoint model

$$\hat{\lambda}(t'') = \int_{t''}^T \mathbf{R}^T(\hat{t}, t'') \mathbf{H}^T(\hat{t}) \boldsymbol{\beta}^n d\hat{t} \quad (3.38)$$

and compute the corrections $\mathbf{e}(t')$

$$\mathbf{e}(t') = \int_{t_0}^T \mathbf{C}(t', t'') \hat{\lambda}(t'') dt'' \quad (3.39)$$

Finally we update the model state

$$\hat{\mathbf{u}}^n(t) = \underbrace{\mathbf{R}(t_0, t) \hat{\mathbf{u}}_0 + \int_{t_0}^t \mathbf{R}(t', t) \{N(\mathbf{u}_B) + \mathbf{F}(t')\} dt'}_{\mathbf{u}_F^n(t)} + \int_{t_0}^t \mathbf{R}(t', t) \mathbf{e}(t') dt' \quad (3.40)$$

where the first two term on the right hand side represent $\mathbf{u}_F^n(t)$, which is corrected by introducing the integral term containing $\mathbf{e}(t')$. If the estimate $\hat{\mathbf{u}}^n(t)$ is not satisfactory we proceed to the next iteration (3.31) and use $\hat{\mathbf{u}}^n(t)$ as the basic state for the linearization of the tangent and adjoint models instead of $\mathbf{u}_B(t)$. Note that for every n the initial value of the prior is untouched. Each n is the solution of an inverse problem.

This method of solution is the IRM and is equivalent to solving the nonlinear Euler Lagrangian equations with an iterative approach for the minimum of the cost function (Egbert et al., 1994; Chua and Bennett, 2001; Bennett, 2002).

4. Forcing terms in tangent linear and adjoint equations

An important practical consideration in the implementation of the inner loop (3.33) is the symmetry of the covariance matrix $\widehat{\mathbf{R}}(\hat{t}, \hat{t})$ (the reproducing kernel), which appears in the evaluation of the action of the stabilized representer matrix $\widehat{\mathbf{P}}$ on the vector $\boldsymbol{\psi}$ according to:

$$\widehat{\mathbf{P}}\boldsymbol{\psi} = \int_{t_0}^T \mathbf{H}(\hat{t}) \int_{t_0}^T \widehat{\mathbf{R}}(\hat{t}, \hat{t}) \mathbf{H}^T(\hat{t}) \boldsymbol{\psi} d\hat{t} d\hat{t} + \mathbf{C}_\varepsilon \boldsymbol{\psi} \quad (4.1)$$

where

$$\widehat{\mathbf{R}}(\hat{t}, \hat{t}) \equiv \int_{t_0}^{\hat{t}} \int_{t_0}^{\hat{t}} \mathbf{R}(t', \hat{t}) \mathbf{C}(t', t'') \mathbf{R}^T(\hat{t}, t'') dt'' dt' \quad (4.2)$$

Algebraically it is readily seen that $\widehat{\mathbf{R}}$ is symmetric in space and in time so that $\widehat{\mathbf{R}}(t_1, t_2) = \widehat{\mathbf{R}}^T(t_1, t_2) = \widehat{\mathbf{R}}(t_2, t_1)$. It is highly desirable to preserve to symmetry to numerical accuracy, where the action of $\widehat{\mathbf{R}}$ is evaluated using the adjoint model integration forced at observation locations followed by an integration of the perturbation tangent model forced with the convolved adjoint solution (see Eq. (3.33)). In inverse ROMS this symmetry is achieved by introducing the forcing terms in both the adjoint and tangent models as impulses added to the state vector. This is different from the more traditional time stepping of the right hand side forcing terms. This implementation follows from the way AD-ROMS, TL-ROMS and RP-ROMS are derived from the NL-ROMS (Moore et al., 2004). To illustrate this point let us assume an assimilation window of 4 time steps from $[t_0, t_3]$ and compute the inner loop for a set of forcing impulses $\mathbf{f}^\dagger(t_n)$. For simplicity and without loss of generality let us also assume that the symmetric covariance matrix in (4.2) is diagonal in space and time, with unit variance $\mathbf{C}(t_m, t_n) = \delta(t_m - t_n)$, implying that errors in the initial condition, boundary conditions and model dynamics are uncorrelated. The solution $\boldsymbol{\lambda}(t_n)$ of the adjoint model integration forced with impulses $\mathbf{f}^\dagger(t_n)$ is obtained by adding the forcing $\mathbf{f}^\dagger(t_n)$ to the adjoint state $\boldsymbol{\lambda}(t_n)$ at the beginning of time step n with no additional multiplicative factors and then performing the time step as follows:

$$\begin{aligned}
\boldsymbol{\lambda}(t_3) &= 0 \\
\boldsymbol{\lambda}(t_2) &= \mathbf{R}^T(t_3, t_2) [\boldsymbol{\lambda}(t_3) + \mathbf{f}^\dagger(t_3)] \\
\boldsymbol{\lambda}(t_1) &= \mathbf{R}^T(t_2, t_1) [\boldsymbol{\lambda}(t_2) + \mathbf{f}^\dagger(t_2)] \\
\boldsymbol{\lambda}(t_0) &= \mathbf{R}^T(t_1, t_0) [\boldsymbol{\lambda}(t_1) + \mathbf{f}^\dagger(t_1)]
\end{aligned} \tag{4.3}$$

where $\mathbf{R}^T(t_{n+1}, t_n)$ represents an adjoint model time step. The convolution of the adjoint solution is just $\sum_{n=0}^3 \mathbf{C}(t_m, t_n) \boldsymbol{\lambda}(t_n) = \sum_{n=0}^3 \delta(t_m - t_n) \boldsymbol{\lambda}(t_n) = \boldsymbol{\lambda}(t_m)$ consequently in the tangent model the forcing terms will appear as

$$\begin{aligned}
\boldsymbol{\tau}(t_0) &= 0 \\
\boldsymbol{\tau}(t_1) &= \mathbf{R}(t_0, t_1)[\boldsymbol{\tau}(t_0) + \boldsymbol{\lambda}(t_0)] \\
\boldsymbol{\tau}(t_2) &= \mathbf{R}(t_1, t_2)[\boldsymbol{\tau}(t_1) + \boldsymbol{\lambda}(t_1)] \\
\boldsymbol{\tau}(t_3) &= \mathbf{R}(t_2, t_3)[\boldsymbol{\tau}(t_2) + \boldsymbol{\lambda}(t_2)]
\end{aligned} \tag{4.4}$$

Let us now check the symmetry of the reproducing kernel $\widehat{\mathbf{R}}(t_3, t_3)$. This is done by forcing the adjoint model (4.3) with $\mathbf{f}^\dagger(t_n) = \boldsymbol{\delta}(t_n - t_3)$ and integrating the tangent model (4.4) up to t_3 forced with the adjoint solution. After substitution we obtain

$$\begin{aligned}
\widehat{\mathbf{R}}(t_3, t_3) &= \mathbf{R}(t_2, t_3)\mathbf{R}(t_1, t_2)\mathbf{R}(t_0, t_1)\boldsymbol{\lambda}(t_0) + \mathbf{R}(t_2, t_3)\mathbf{R}(t_1, t_2)\boldsymbol{\lambda}(t_1) + \mathbf{R}(t_2, t_3)\boldsymbol{\lambda}(t_2) \\
&= \mathbf{R}(t_0, t_3)\boldsymbol{\lambda}(t_0) + \mathbf{R}(t_1, t_3)\boldsymbol{\lambda}(t_1) + \mathbf{R}(t_2, t_3)\boldsymbol{\lambda}(t_2) \\
&= \underbrace{\mathbf{R}(t_0, t_3)\mathbf{R}^T(t_3, t_0)}_{\text{symmetric}}\boldsymbol{\delta}(t_3) + \underbrace{\mathbf{R}(t_1, t_3)\mathbf{R}^T(t_3, t_1)}_{\text{symmetric}}\boldsymbol{\delta}(t_3) + \underbrace{\mathbf{R}(t_2, t_3)\mathbf{R}^T(t_3, t_2)}_{\text{symmetric}}\boldsymbol{\delta}(t_3)
\end{aligned} \tag{4.5}$$

where we make use of the equality $\mathbf{R}(t_2, t_3)\mathbf{R}(t_1, t_2)\mathbf{R}(t_0, t_1) \equiv \mathbf{R}(t_0, t_3)$. The matrix $\widehat{\mathbf{R}}(t_3, t_3)$ is clearly symmetric as it is the sum of symmetric matrices.

Although this approach preserves the symmetry of the covariance matrix $\widehat{\mathbf{R}}$ and the inner loop, it is very expensive and impractical for large application as it requires saving the adjoint solution at every time step. Therefore, a modified version of this approach is implemented in inverse ROMS which maintains the symmetry without saving the adjoint solution at each time step. To illustrate how this is done consider the case when the adjoint solution $\boldsymbol{\lambda}(t_1)$ has not been saved. If we linearly interpolate $\boldsymbol{\lambda}(t_1) = [\boldsymbol{\lambda}(t_0) + \boldsymbol{\lambda}(t_2)]/2$ and use this to force the tangent model, we obtain

$$\begin{aligned}
\widehat{\mathbf{R}}(t_3, t_3) &= \mathbf{R}(t_0, t_3)\boldsymbol{\lambda}(t_0) + \mathbf{R}(t_1, t_3)\frac{\boldsymbol{\lambda}(t_0) + \boldsymbol{\lambda}(t_2)}{2} + \mathbf{R}(t_2, t_3)\boldsymbol{\lambda}(t_2) \\
&= \underbrace{\mathbf{R}(t_0, t_3)\mathbf{R}^T(t_3, t_0)}_{\text{symmetric}}\boldsymbol{\delta}(t_3) + \underbrace{\mathbf{R}(t_1, t_3)\frac{\mathbf{R}^T(t_3, t_0) + \mathbf{R}^T(t_3, t_2)}{2}}_{\text{non symmetric}}\boldsymbol{\delta}(t_3) + \underbrace{\mathbf{R}(t_2, t_3)\mathbf{R}^T(t_3, t_2)}_{\text{symmetric}}\boldsymbol{\delta}(t_3)
\end{aligned} \tag{4.6}$$

The second term in $\widehat{\mathbf{R}}(t_3, t_3)$ is not symmetric. However, if we approximate the tangent propagator $\mathbf{R}(t_1, t_3) = [\mathbf{R}(t_0, t_3) + \mathbf{R}(t_2, t_3)]/2$ and substitute in (4.6) we retrieve a symmetric

$$\widehat{\mathbf{R}}(t_3, t_3) = \underbrace{\mathbf{R}(t_0, t_3)\mathbf{R}^T(t_3, t_0)}_{\text{symmetric}}\boldsymbol{\delta}(t_3) + \underbrace{\frac{\mathbf{R}(t_0, t_3) + \mathbf{R}(t_2, t_3)}{2}\frac{\mathbf{R}^T(t_3, t_0) + \mathbf{R}^T(t_3, t_2)}{2}}_{\text{symmetric}}\boldsymbol{\delta}(t_3) + \underbrace{\mathbf{R}(t_2, t_3)\mathbf{R}^T(t_3, t_2)}_{\text{symmetric}}\boldsymbol{\delta}(t_3) \quad (4.7)$$

The symmetry of the second term is evident if one considers the symmetric matrix $[\mathbf{A} + \mathbf{B}][\mathbf{A} + \mathbf{B}]^T = [\mathbf{A} + \mathbf{B}][\mathbf{A}^T + \mathbf{B}^T]$. By regrouping terms and substituting the adjoint solution $\boldsymbol{\lambda}(t_n)$ we obtain

$$\widehat{\mathbf{R}}(t_3, t_3) = \mathbf{R}(t_0, t_3)\left[\boldsymbol{\lambda}(t_0) + \frac{\boldsymbol{\lambda}(t_0) + \boldsymbol{\lambda}(t_2)}{4}\right] + \mathbf{R}(t_2, t_3)\left[\boldsymbol{\lambda}(t_2) + \frac{\boldsymbol{\lambda}(t_0) + \boldsymbol{\lambda}(t_2)}{4}\right] \quad (4.8)$$

which shows that the symmetry can be preserved by forcing the tangent model by a linear combination of the adjoint solutions at the time steps when the adjoint solution is saved.

This example can be generalized to show that if the adjoint solution is saved every M time steps, the tangent model is also forced every M time steps with a linear combination of the adjoint solutions given by:

$$t_n : \quad \frac{2M^2 + 1}{3M}\boldsymbol{\lambda}(t_n) + \frac{M^2 - 1}{6M}[\boldsymbol{\lambda}(t_{n+M}) + \boldsymbol{\lambda}(t_{n-M})]. \quad (4.9)$$

The initial and final time steps are special cases:

$$\begin{aligned} t_0 : \quad & \frac{(M+1)(2M+1)}{6M}\boldsymbol{\lambda}(t_0) + \frac{M^2-1}{6M}\boldsymbol{\lambda}(t_{0+M}) \\ t_N : \quad & \frac{(M+1)(2M+1)}{6M}\boldsymbol{\lambda}(t_N) + \frac{M^2-1}{6M}\boldsymbol{\lambda}(t_{N-M}) \end{aligned} \quad (4.10)$$

5. Application to Coastal Upwelling with complex topography

Various tests have been performed to ensure that the 3D implementation of inverse ROMS is correct. These include tests of the symmetry of the representer matrix (precise to 1.0e-11 on average), iterations for the convergence of the representer model and synthetic data assimilation experiments using the 3D double gyre case, which is a standard test case provided within the ROMS framework. The 3D double gyre case has been used also to perform a successful chi-square test following the approach of Muccino et al (2004). However, ROMS is a complex code with many options and it is difficult to ensure that all the model options are

working properly until tested. Given the wide use of ROMS in coastal application we present here a realistic assimilation experiment for a coastal upwelling baroclinic system with complex topography characterized by strong nonlinearity and mesoscale variability. This configuration allows assessing the performance of the assimilation system using the most common model configuration options that are enabled in real coastal application. The assimilation experiment will be conducted using synthetic observations extracted from a given realization of the nonlinear forward integration.

5.1 Model Configuration

ROMS was configured in a 440x220 km domain (Fig. 1a) with periodic open boundary conditions in the north and south, and closed boundary conditions in the east and west. The topography (Fig. 1a) is characterized by a shelf region along the eastern boundary with canyons and seamounts. As we progress towards the western boundary there is a slope region where the bathymetry deepens to a maximum of 600 m. The horizontal resolution of the model is 10 km, which is a typical eddy permitting resolution used in models of the eastern boundary upwelling circulations. In the vertical, 10 layers are stretched from top to bottom with enhanced resolution at the surface and bottom boundary. The stretching parameters for the s-coordinate system are 6 and 0.4 for the surface and bottom boundary respectively. The meridional gradient in planetary vorticity is comparable to that at 32N. The NL-ROMS uses all the most common options used in high resolution coastal model configurations except for nested open boundary conditions (Miller et al., 2000; Marchesiello et al., 2002; Di Lorenzo, 2003). An example of an inverse ROMS application with nested open boundary conditions is provided in Di Lorenzo et al. (2006) where observations in the California Current are assimilated in a regional nested version of ROMS.

At the surface the model is forced with a seasonal cycle of alongshore and cross-shore wind stresses. The spatial and temporal evolution of the wind stress is taken from a monthly climatology of the NCEP reanalysis (Kistler et al., 2001) for a patch of ocean along the California Current centered around 32N and 123W. The surface fluxes of heat and freshwater are set to zero, so the seasonal cycle of the model is only controlled by mechanical forcing. The model salinity is used as a passive tracer and density is controlled only by temperature through the linear equation of state. The initial temperature is uniform in the horizontal and stratified in the vertical. Stratification is set based on observations from California Cooperative Ocean Fisheries Investigation (CalCOFI) at 32N and 123W. After a 3 year spin-up the model circulation is characterized by a typical upwelling structure in the vertical (Fig. 1b) with strong baroclinicity and equatorward flow. The dynamics are nonlinear and the flow field exhibits mesoscale horizontal activity around the irregular topography with typical filament structures in

the tracer observed in upwelling systems (see discussion of inverse solution in section 5.5 for a more thorough description of the horizontal flow).

5.2 Assimilation experimental setup and synthetic observations

Two different sets of synthetic observations are generated by sampling the NL-ROMS solution during JAN 1 through JAN 11, YEAR=3. This 10 day period will be referred to as the assimilation window or hindcast period. In the first set, we sample temperature and horizontal velocities of the nonlinear model with a high resolution array in both horizontal (Fig. 1a, black x) and vertical (Fig. 1b, black x on temperature section). The horizontal sampling resolution is 20 km while in the vertical it is variable, 20 m close to the surface and 100 m in deep waters. The array is fully sampled during days 2, 6 and 10. We refer to this sampling array as the HIRES. The second set is obtained by sampling the same horizontal and vertical array only once during the entire 10 days. In this second set, which we refer to as COARSE, observations are available in the southern portion of the domain during DAY=1, and as the integration progresses forward in time observations become available to the north. At DAY=10 the entire array will have been sampled. The COARSE sampling array is meant to mimic an oceanographic cruise track taking CTD casts as the ship moves from south to north. As will be discussed in the next section the COARSE array, in contrast with the HIRES, introduces a spatial and temporal aliasing of the flow field.

5.3 Representer functions and sampling array design

To assess if the sampling array is adequate to capture the important dynamical information of the flow field, we compute the space-time cross-covariances between the observations and the entire model state. This is a measure of the ability of the observations to observe the flow field in space and time. The computation is done using the AD-ROMS and TL-ROMS in the following way. Consider the model state for the perturbations $\mathbf{s}(t)$ and its cross-covariance $\langle \mathbf{s}(\hat{t})\mathbf{s}^T(\hat{t}) \rangle$. The state $\mathbf{s}(t)$ evolves according to the tangent linear $\mathbf{s}(t) = \mathbf{R}(t_0, t)\mathbf{s}(t_0)$ so that:

$$\langle \mathbf{s}(\hat{t})\mathbf{s}^T(\hat{t}) \rangle = \left\langle \mathbf{R}(t_0, \hat{t})\mathbf{s}(t_0) \left(\mathbf{R}(t_0, \hat{t})\mathbf{s}(t_0) \right)^T \right\rangle = \mathbf{R}(t_0, \hat{t}) \langle \mathbf{s}(t_0)\mathbf{s}^T(t_0) \rangle \mathbf{R}^T(\hat{t}, t_0) = \mathbf{R}(t_0, \hat{t})\mathbf{C}(t_0, t_0)\mathbf{R}^T(\hat{t}, t_0) \quad (5.1)$$

where \mathbf{R} and \mathbf{R}^T are the propagators TL-ROMS and AD-ROMS respectively, and $\langle \mathbf{s}(t_0)\mathbf{s}^T(t_0) \rangle = \mathbf{C}(t_0, t_0)$ is the spatial cross-covariance of the field at zero time lag, corresponding

to JAN 1 in the assimilation window. If we assume that $\mathbf{C}(t_0, t_0)$ is a diagonal matrix with unit variance \mathbf{I} , then the columns of $\langle \mathbf{s}(\hat{t}) \mathbf{s}^T(\hat{t}) \rangle$ reveal the role played by the dynamics, which is to shape the space-time covariance. This information is analogous to that obtained from the columns of the full representer matrix $\widehat{\mathbf{R}}(\hat{t}, \hat{t})$ (3.26), for the case when $\mathbf{C} \equiv \mathbf{C}(t_0, t_0) = \mathbf{I}$, and provides an immediate physical understanding of the columns of the representer matrix, also called representer function, as space-time cross-covariances between the observations and the entire model state.

To compute representer functions in inverse ROMS we integrate the AD-ROMS forced with a delta function at the space and time location of the observations. We then convolve the adjoint solution at time t_0 with $\mathbf{C}(t_0, t_0)$ and use the convolved state as initial condition for TL-ROMS. The solution from TL-ROMS represents the cross-covariance relative to the chosen observation. This operation is part of the inverse ROMS inner loop (3.33). The panels on Fig. 2 show the cross-covariance of two cross-shore velocity observations $U(x, y, z, t = 6d)$, located at the black (x). For example, in the first column of Fig. 2 the covariance $\langle U(x, y, z, t = 6d) \mathbf{U}^T \rangle$ provides information on the horizontal scales resolved by the velocity observations at DAY=6. The cross-covariances $\langle U(x, y, z, t = 6d) \mathbf{T}^T \rangle$, $\langle U(x, y, z, t = 6d) \mathbf{V}^T \rangle$ show gradients in temperature and alongshore velocity, which are the signature of the dynamical constraint imposed by the model. The stirring action of the flow field becomes more evident when looking at the cross-covariance between $U(x, y, z, t = 6d)$ and the other state variables at future times (DAY=10, Fig. 2, column 2). For example, knowledge of $U(x, y, z, t = 6d)$ will lead information of the temperature downstream at DAY=10 (the flow is moving towards the south).

Using the model dynamics to shape the covariances is a very powerful tool that can be exploited in a systematic way for array design and adaptive observation sampling. However in this paper, we only use the representer functions as a guide to the spatial and temporal scales of the flow field statistics. For the upwelling test case, we determine that the HIRES sampling array is adequate to collect information of the flow field in both space and time. In contrast, the COARSE resolution has a temporal aliasing because of the fast moving timescales of the flow. As we will show later the persistence timescale is less than 5 days. This means that in a 10 day assimilation window, information in the initial conditions is no longer a good estimate of the flow field.

5.4 Error covariances for the model and observations

In order to proceed with the assimilation experiment we must specify the covariances of the observational error \mathbf{C}_e and of the corrections to the state $\mathbf{C}(t',t'')$, also referred to as model error covariance. These covariances appear in the cost function (3.6). For the observations we assume a signal to noise variance ratio of 10 and use this to define the observational error variances. For the standard deviation of the signal we use 2 °C for temperature, 0.3 m s⁻¹ for velocity and 0.3 m for surface elevation. These values are determined from the statistics of the flow field from a longer integration of the NL-ROMS. We also assume that errors in each observations are uncorrelated, which renders \mathbf{C}_e a diagonal matrix. For $\mathbf{C}(t',t'')$ we assume a Gaussian covariance in space and white in time. The decorrelation length scales are 30 km in the horizontal and 50 m in the vertical. For the diagonal elements of $\mathbf{C}(t',t'')$ we assume that the corresponding error in the state variable has variance equal to the one computed from the statistics of the nonlinear integration. With this assumption we implicitly assume that the model error and initial condition errors $\mathbf{C}(0,0)$ have the same statistics. This assumption is discussed further in section 5.5, together with the an explanation of the sources errors. Boundary conditions are prescribed to be the same in all the experiments and therefore assumed to be perfect. The convolution of $\mathbf{C}(t',t'')$ with the adjoint state variables in the inner loop computed using the diffusion operator approach described in Weaver and Courtier (2001). This approach essentially solves the diffusion equation as a way to impose the Gaussian shape of the covariance by spreading in space the information of the model grid points over the desired length scale. The decorrelation length scale is controlled by varying the number of time steps. The use of this approach in the representer based inversion is further illustrated in Chua and Bennett (2001) and Muccino et al. (2006).

The role of $\mathbf{C}(t',t'')$ is to smooth the adjoint field in the inner loop (3.33) and condition the inverse of the representer matrix, the first term in (3.33), by constraining the spatial and temporal scales of the corrections of the state. The inverse solution will strongly depend on the functional form of $\mathbf{C}(t',t'')$. In this initial implementation of inverse ROMS, $\mathbf{C}(t',t'')$ has no cross terms between different variables of the state. The cross-covariance terms and dynamical constraint are imposed by AD-ROMS and TL-ROMS when computing the representer matrix. We find that this choice of covariance is acceptable for the upwelling test case. However, it is clear that the dynamical constraints and the space-time stretching of $\mathbf{C}(t',t'')$ (which correspond to the representer functions) do not always lead to a good inverse solution. This is particularly true when observations are sparse and the 2nd term in the cost function (3.6), the model error term, plays a more substantial role in constraining the inverse solution. For example, if we were

to assimilate sea surface elevation only, the block diagonal Gaussian formulation of $\mathbf{C}(t',t'')$ will not allow for the dynamical balances between sea surface height, temperature and salinity via the tangent and adjoint models. This would result in a poor fit of the data. The specification of more appropriate forms for model error covariances like $\mathbf{C}(t',t'')$ has been the focus of numerous studies that aim to impose additional dynamical constraints (e.g. the geostrophic balance and static stability) or statistical constraints derived from the flow field (e.g. the use of vertical multivariate Empirical Orthogonal Functions) (Courtier et al., 1998; Lorenc, 1997; 2003; Parrish et al. 1997; Weaver and Courtier, 2001; Derber and Bouttier, 1999; Dobricic et al., 2006; Ricci et al., 2005). A full discussion of $\mathbf{C}(t',t'')$ is beyond the scope of this paper and one needs to explore what is more appropriate for the dynamics of the particular flow field of interest during the assimilation setup. Di Lorenzo et al. (2006) addresses this issue in more depth by applying inverse ROMS to the assimilation of coastal eddies in the Southern California Current System.

5.5 Weak and strong constraint Inverse solutions

Two set of experiments are performed using the HIRES and COARSE sampling array as summarized in Table 1. For each sampling array we compute the inverse solution that minimizes the model minus observation misfit using both the weak and strong constraint formulation within inverse ROMS. In the strong constraint case, only the initial conditions of the model act as control parameters. The synthetic observations are derived applying the sampling array to the NL-ROMS solution shown in Fig. 3 (column one). We refer to this as the “true” solution. During the 10 day assimilation window, the “true” solution is characterized by the development of two centers of cyclonic circulation south of the topographic promontories.

The initial basic state $\mathbf{u}_B(t)$ is obtained by integrating the nonlinear model initialized with the climatological condition for January (Fig. 3, column 2). The basic state trajectory exhibits similar features as the “true” solution with evidence of two centers of mean cyclonic circulation between the topographic promontories superimposed on a general east-west temperature gradient and strong southward flow (0.7 m s^{-1}). However in the basic state solution the cyclonic features are displaced southward, and the filament structures in the temperature field are not captured. This basic trajectory is then used to produce the “first guess” $\mathbf{u}_F^n(t)$ using the linearized model RP-ROMS. This first guess has errors in the initial condition, specified from climatology, and errors in the model dynamics arising from the linearization used in the full state tangent linear model RP-ROMS. This error exist because the synthetic observations are generated using NL-ROMS and therefore contain dynamics that are not explicitly resolved in RP-ROMS. As discussed in the previous section, we assume that the model error terms in the

state vector have similar statistics as the errors in the initial condition. An a posteriori check of the inverse solution will show that such an assumption is acceptable for the experiments presented here; however assumptions on model errors in real applications are difficult and must be carefully considered depending on the type of application.

The inverse solutions for the weak and strong constraint using the HIRES sampling array are also shown in Fig. 3 (column 3 and 4). Both inverse solutions are able to recover the general structure of the flow field, its filaments, and the timing and spatial location of the two cyclonic centers. The reduction of variance in the misfit between the synthetic observations and model are shown in Fig. 4. The black line shows the misfit between the observation and the “first guess” , and the gray line between observations and the inverse solution. In the HIRES case we find that the weak formulation of inverse ROMS is able to reduce the error variance by over 97%. In the strong formulation the error variance reduction is smaller ranging from 76% to 87%. This is consistent with the fact that in the strong case, (a) the inverse solution has fewer degrees of freedom when fitting the data, and (b) the model is assumed to be error free and the inverse solution cannot account for the model dynamical errors. Indeed inspection of the upper ocean temperature maps (Fig. 3) shows more structure in the initial condition for the strong constraint solution in contrast with the weak. Some of these features are physically incorrect (e.g. the hot spots along the eastern boundary). These hot spots result from aliasing the model errors into corrections to the initial condition. In the weak constraint, where these errors are explicitly accounted for, the fields remain smoother throughout the assimilation window.

These solutions were obtained with approximately 120 iterations of the inner loop and 1 iteration for the outer loop. In principal one could try to perform more outer loop iteration (updates to the basic state) so that the linearized dynamics of the RP-ROMS converge toward the true nonlinear dynamics. However in this upwelling test case, further iterations of the outer loop do not improve the inverse solution. As will be shown in section 5.7 the linearized model is very unstable, and iterations of the RP-ROMS do not guaranteed convergence to the true nonlinear model state in the case of more highly nonlinear flow fields.

The solutions using the COARSE sampling array (Fig. 4) show higher reduction in error variance, which is consistent with the fact that we have fewer observations to fit and therefore less constraints on the circulation. The spatial evolution of the upper ocean temperature and of the flow field (not shown) resembles that of the HIRES case (Fig. 3). This suggests that inverse ROMS is able to reconstruct the flow field dynamics from a set of temporally and spatially aliased observations. But how good is this reconstruction? We address this question in the following section.

5.6 Independent verification of hindcast and forecast skill

To quantify the quality of the inverse solutions we compute the hindcast and forecast skill of the model by comparing with a set of independent observations (i.e. observations that were not assimilated into the model) available from the “true” solution. The skill score is defined in terms of RMS differences according to:

$$SKILL(\mathbf{s}) = 1 - \frac{(\mathbf{s}_{\text{true}} - \mathbf{s})^T (\mathbf{s}_{\text{true}} - \mathbf{s})}{(\mathbf{s}_{\text{true}} - \mathbf{s}_{\text{clima}})^T (\mathbf{s}_{\text{true}} - \mathbf{s}_{\text{clima}})} \quad (5.2)$$

where \mathbf{s} is the state vector of the model for which we evaluate the skill, \mathbf{s}_{true} is the “true” state and $\mathbf{s}_{\text{clima}}$ is the climatology. With this definition, a skill score of 1 implies a perfect match with the “true” solution and a skill of 0 implies that the model is not better than climatology. Fig. 5 (top panels) show that both the weak and strong constraint inverse solution for the HIRES case possess reasonable skill during the hindcast window. Forecast skill exceeds that of climatology for up to 20 days after the model has assimilated the last observation. In general the weak constraint case retains higher and longer skill over the full 30 day period. The forecast is performed using NL-ROMS initialized with the inverse solution at DAY=10.

We now compare the skill against the natural persistence timescale of the flow field. This is a measure of the ability of the inverse solution to correct the dynamical trajectory of the model. The persistence skill of the observations is computed by taking only the available synthetic observations assimilated by the model at DAY=10 and computing a spatial objective map to interpolate at all other locations where the independent observations reside. For this reason the persistence skill at DAY=10 is not 1. This is a fair comparison given that in real applications only observations at particular time and space are available. The objective mapping employs the same spatial decorrelations length scales assumed for the covariance $\mathbf{C}(t', t'')$ so that its lack of perfect skill can be interpreted as a measure of the suboptimal nature of the statistical assumptions in the model error covariance. The fact that neither the strong or the weak case possess a higher level of skill at DAY=10 may imply that either (a) the corrections to the state have scales smaller than those imposed via $\mathbf{C}(t', t'')$, or (b) that the modification of $\mathbf{C}(t', t'')$ by the model dynamics is not sufficient to recover a better data-model covariance implicit in the representer matrix.

The persistence skill score approaches zero after approximately 5 days because of the strong advection characterizing the flow field. Both the weak and strong constraint formulation maintain positive skill 10-15 days beyond persistence. This suggests that the inverse method was able to properly initialize the model dynamics during the assimilation hindcast window, rather

than just fitting the observations. In the more realistic case of assimilation of spatially and temporally aliased observations, the COARSE case, the forecast and hindcast skill are much reduced (Fig. 5, bottom panels). The weak and strong constraint formulation do not show substantial differences, the weak having slightly longer forecast skill. However, both the weak and strong case still perform better than the persistence of the observations, which in this case is characterized by a very low skill because of the spatial and temporal aliasing in the sampling array.

The measure of skill used for the comparison is strict and one should inspect the spatial pattern of the flow field in the forecast window (Fig. 6). This reveals that both the weak and strong formulation, in the COARSE case, are a substantial improvement over the basic state. The location of the cyclonic centers is shifted slightly southward but is consistent with the “true” solution. The filament structures are also captured. The HIRES forecast spatial pattern (not shown) shows a more dramatic improvement capturing the amplitude and timing of the cyclonic centers almost exactly.

5.7 Convergence of linearized dynamics in the outer loop

One important assumption in the indirect representer method is that the linearized model state (the solution of RP-ROMS) will converge to the true nonlinear state when iterating the RP-ROMS by updating the basic state used for the linearization. This is achieved by updating the basic state after each iteration with the new improved state obtained by the previous assimilation cycle.

Our experience is that this assumption is true for systems that are more close to the linear regime (e.g. the 3D double gyre) but fails when nonlinearity becomes more important. Fig. 7 shows the skill, as previously defined in (5.2), obtained by integrating the RP-ROMS starting from the “true” initial condition and using either climatology (black continuous line with dots) or the “true” forward trajectory (black continuous line) as the basic state for the linearized dynamics. It is clear that in both cases the skill is very poor by DAY=10. In theory the integration using the true state as basic state, should be very close to the truth. This is obviously not the case.

Another important aspect of this comparison is that the trajectory obtained using the weak constraint formulation in the HIRES case shows the highest skill. This suggests that for this upwelling test case the RP-ROMS will never converge to the true state by increasing the number of outer loop iterations (indeed a brute force attempt to do so makes the RP-ROMS blow up after 4 iterations). As a consequence the dynamics should always be imposed as weak constraint.

The lack of convergence derives from the fact that the RP-ROMS is highly unstable. This implies that the right hand side correction terms from the weak constraint inverse solution, are not only trying to improve the fit with the observations but are also damping the linear instabilities of RP-ROMS. This explains why the strong constraint case, which does not allow for these forcing terms, performs poorly compared to the weak constraint. In Di Lorenzo et al. (2006) different formulations of the outer loop are explored. In one case RP-ROMS is modified from its original implementation to include a nudging term to the solution of the previous iteration (Bennett, 2002). This limits the growth rate of the RP-ROMS linear instabilities. In another case RP-ROMS is replaced with the NL-ROMS. Preliminary results with these approaches appear to greatly improve the inverse solutions.

6. Summary

We have described in section 3, the development of the inverse Regional Ocean Modeling System (inverse ROMS), a 4DVAR data assimilation system for high-resolution basin-wide and coastal oceanic flows. Inverse ROMS utilizes the recently developed perturbation tangent linear, representer tangent linear and adjoint models of the ROMS (Moore et al., 2004), to implement an indirect representer-based inverse modeling system (Chua and Bennett, 2001). The assimilation can be performed either under the perfect model assumption (strong constraint) or by also allowing for errors in the model dynamics (weak constraint). For the weak constraint case, the tangent linear and representer tangent linear models are modified (see section 4) to include additional forcing terms on the right hand side of the model equations. These terms are needed to account for errors in the model dynamics.

We also presented a realistic application of inverse ROMS for a 3D baroclinic coastal upwelling system with complex bottom topography (section 5). In this example, the flow field is nonlinear and characterized by mesoscale activity as evident from the filamentary and cyclonic structures in the circulation (Fig. 3). Synthetic observations of upper ocean (0-450m) temperatures and currents with a high resolution sampling array (HIRES) were assimilated first for a 10 day window. In this case, both the strong and weak constraint inverse solutions were able to greatly reduce the initial error variance by 97% and 80% respectively (section 5.5, Fig. 4). We also found that both solutions exhibit relatively high forecast skill (section 5.6) when used to initialize the nonlinear model at the end of the assimilation window. Significant forecast skill was found up to 10-20 days after the last observation is assimilated and is higher than the persistence timescale of the flow, which for this upwelling regime is less than 5 days (Fig. 5).

The same experiment was repeated using an observing array that is both spatially and temporally aliased. For this case, both the strong and weak constraint possess similar levels of hindcast and forecast skill, although the weak case was slightly better. During the forecast, the

skill was not as high as in the HIRES case, however the spatial pattern correlation with the true is still very high when compared to the first guess (Fig. 6). These results suggest that the indirect representer method with inverse ROMS is able to extract the dynamically active information from the observations during the hindcast window and generate a good initialization for the forecast.

We also found that the use of the linearized model (RP-ROMS) in an iterative approach (the outer loop) does not necessarily converge to the solution obtained by the nonlinear model (section 5.7, Fig. 7). The RP-ROMS is linearly unstable when the flow field is very nonlinear. This implies that in the assimilation window the corrections provided by the inverse solution need also to damp the linear instabilities that develop in the RP-ROMS. In Di Lorenzo et al. (2006) different formulations of the outer loop are explored, in which either the linear instability of RP-ROMS are damped by including a nudging term to the solution of the previous iteration (Bennett, 2002), or the RP-ROMS is replaced with NL-ROMS. This second approach is similar to Courtier (1997). Preliminary results suggest that these approaches greatly improve the inverse solutions.

Applications of inverse ROMS using real ocean observations are currently being performed for the Southern California Bight (Di Lorenzo et al., 2006) and for the Intra-Americas Seas (Powell et al., pers. comm.).

7. Acknowledgments

This research was supported at different institutions by the following grants: ONR N00014-05-10365, NSF OCE0121176 OCE0121506, ONR N00014-01-0209 N00014-05-1-0366 N00014-05-1-0363 and NSF-ITR OCE0121332

References

- Anderson, D. L. T., J. Sheinbaum, and K. Haines, 1996: Data assimilation in ocean models. *Reports on Progress in Physics*, **59**, 1209-1266.
- Arango, H., A. M. Moore, E. Di Lorenzo, B. D. Cornuelle, A. J. Miller, and D. J. Neilson, 2006: The ROMS tangent linear and adjoint models: A comprehensive ocean prediction and analysis system. *IMCS, Rutgers Tech. Reports*, in preparation.
- Bell, M. J., R. M. Forbes, and A. Hines, 2000: Assessment of the FOAM global data assimilation system for real-time operational ocean forecasting. *Journal of Marine Systems*, **25**, 1-22.
- Bennett, A. F., 1992: *Inverse Method in Physical Oceanography*. Cambridge University Press, 346 pp.
- , 2002: *Inverse Modeling of the Ocean and Atmosphere*. Cambridge University Press, 225 pp.
- Bennett, A. F. and M. A. Thorburn, 1992: The Generalized Inverse of a Nonlinear Quasi-Geostrophic Ocean Circulation Model. *Journal of Physical Oceanography*, **22**, 213-230.
- Bennett, A. F., B. S. Chua, D. E. Harrison, and M. J. McPhaden, 1998: Generalized inversion of tropical atmosphere-ocean data and a coupled model of the tropical Pacific. *Journal of Climate*, **11**, 1768-1792.
- , 2000: Generalized inversion of Tropical Atmosphere-Ocean (TAO) data and a coupled model of the tropical Pacific. Part II: The 1995-96 La Nina and 1997-98 El Nino. *Journal of Climate*, **13**, 2770-2785.
- Bennett, A. F., B. S. Chua, H. E. Ngodock, D. E. Harrison, and M. J. McPhaden, 2006: Generalized inversion of the Gent-Cane model of the tropical Pacific with Tropical Atmosphere-Ocean (TAO) data. *Journal of Marine Research*, **64**, 1-42.
- Bertino, L. and K. A. Lisæter, 2006: The TOPAZ monitoring and prediction system for the Atlantic and Arctic Oceans. *European Operational Oceanography: Present and Future, EuroGOOS Conf. Proc.* in press.
- Chassignet, E. P., H. E. Hurlburt, O. M. Smedstad, G. R. Halliwell, A. J. Wallcraft, E. J. Metzger, B. O. Blanton, C. Lozano, D. B. Rao, P. J. Hogan, and A. Srinivasan, 2006: Generalized vertical coordinates for eddy-resolving global and coastal ocean forecasts. *Oceanography*, **19**, 20-31.
- Chua, B. and A. F. Bennett, 2001: An inverse ocean modeling system. *Ocean Modelling*, **3**, 137-165.
- Cornuelle, B. D., T. K. Chereskin, P. P. Niiler, M. Y. Morris, and D. L. Musgrave, 2000: Observations and modeling of a California undercurrent eddy. *Journal of Geophysical Research-Oceans*, **105**, 1227-1243.
- Courtier, P., 1997: Dual formulation of four-dimensional variational assimilation. *Quarterly Journal of the Royal Meteorological Society*, **123**, 2449-2461.
- Courtier, P., J. Derber, R. Errico, J. F. Louis, and T. Vukicevic, 1993: Important Literature on the Use of Adjoint, Variational-Methods and the Kalman Filter in Meteorology. *Tellus Series a-Dynamic Meteorology and Oceanography*, **45A**, 342-357.
- Curchitser, E. N., D. B. Haidvogel, A. J. Hermann, E. L. Dobbins, T. M. Powell, and A. Kaplan, 2005: Multi-scale modeling of the North Pacific Ocean: Assessment and analysis of simulated basin-scale variability (1996-2003). *Journal of Geophysical Research-Oceans*, **110**.
- De Mey, P. and M. Benkiran, 2002: *A multivariate reduced-order optimal interpolation method and its application to the Mediterranean basin-scale circulation. In : Ocean Forecasting, Conceptual basis and applications.* N. Pinardi and J.D. Woods, Eds., Springer-Verlag, Berlin Heidelberg New York, 472 pp.
- DeMey, P., 1997: Data assimilation at the oceanic mesoscale: A review. *Journal of the Meteorological Society of Japan*, **75**, 415-427.
- Derber, J. and F. Bouttier, 1999: A reformulation of the background error covariance in the ECMWF global data assimilation system. *Tellus Series a-Dynamic Meteorology and Oceanography*, **51**, 195-221.

- Di Lorenzo, E., 2003: Seasonal dynamics of the surface circulation in the Southern California Current System. *Deep-Sea Research Part II-Topical Studies in Oceanography*, **50**, 2371-2388.
- Di Lorenzo, E., M. G. G. Foreman, and W. R. Crawford, 2005: Modelling the generation of Haida Eddies. *Deep-Sea Research Part II-Topical Studies in Oceanography*, **52**, 853-873.
- Di Lorenzo, E., A. J. Miller, D. J. Neilson, B. D. Cornuelle, and J. R. Moisan, 2004: Modelling observed California Current mesoscale eddies and the ecosystem response. *International Journal of Remote Sensing*, **25**, 1307-1312.
- Di Lorenzo, E., A. M. Moore, H. G. Arango, B. D. Cornuelle, and A. J. Miller, 2006: Weak and Strong Constraint Data Assimilation in the inverse Regional Ocean Modeling System (ROMS): sensitivity to error covariance in the Southern California Current eddy field. *Ocean Modelling*, in preparation.
- Dommenget, D. and D. Stammer, 2004: Assessing ENSO simulations and predictions using adjoint ocean state estimation. *Journal of Climate*, **17**, 4301-4315.
- Egbert, G. D. and S. Y. Erofeeva, 2002: Efficient inverse Modeling of barotropic ocean tides. *Journal of Atmospheric and Oceanic Technology*, **19**, 183-204.
- Egbert, G. D., A. F. Bennett, and M. G. G. Foreman, 1994: Topex/Poseidon Tides Estimated Using a Global Inverse Model. *Journal of Geophysical Research-Oceans*, **99**, 24821-24852.
- Eknes, M. and G. Evensen, 1997: Parameter estimation solving a weak constraint variational formulation for an Ekman model. *Journal of Geophysical Research-Oceans*, **102**, 12479-12491.
- Evensen, G., 1994: Inverse Methods and Data Assimilation in Nonlinear Ocean Models. *Physica D*, **77**, 108-129.
- Ferreira, D., J. Marshall, and P. Heimbach, 2005: Estimating eddy stresses by fitting dynamics to observations using a residual-mean ocean circulation model and its adjoint. *Journal of Physical Oceanography*, **35**, 1891-1910.
- Foreman, M. G. G., G. Sutherland, and P. F. Cummins, 2004: M-2 tidal dissipation around Vancouver Island: an inverse approach. *Continental Shelf Research*, **24**, 2167-2185.
- Fox, D. N., W. J. Teague, C. N. Barron, M. R. Carnes, and C. M. Lee, 2002: The Modular Ocean Data Assimilation System (MODAS). *Journal of Atmospheric and Oceanic Technology*, **19**, 240-252.
- Galanti, E., E. Tziperman, M. Harrison, A. Rosati, and Z. Sirkes, 2003: A study of ENSO prediction using a hybrid coupled model and the adjoint method for data assimilation. *Monthly Weather Review*, **131**, 2748-2764.
- Golub, G. H. and C. F. VanLoan, 1982: *Matrix Computations*. John Hopkins University Press, 467 pp.
- Griffin, D. A. and K. R. Thompson, 1996: The adjoint method of data assimilation used operationally for shelf circulation. *Journal of Geophysical Research-Oceans*, **101**, 3457-3477.
- Gunson, J. R. and P. MalanotteRizzoli, 1996: Assimilation studies of open-ocean flows .1. Estimation of initial and boundary conditions. *Journal of Geophysical Research-Oceans*, **101**, 28457-28472.
- , 1996: Assimilation studies of open-ocean flows .2. Error measures with strongly nonlinear dynamics. *Journal of Geophysical Research-Oceans*, **101**, 28473-28488.
- Haidvogel, D. B., H. G. Arango, K. Hedstrom, A. Beckmann, P. Malanotte-Rizzoli, and A. F. Shchepetkin, 2000: Model evaluation experiments in the North Atlantic Basin: simulations in nonlinear terrain-following coordinates. *Dynamics of Atmospheres and Oceans*, **32**, 239-281.
- He, R. Y., D. J. McGillicuddy, D. R. Lynch, K. W. Smith, C. A. Stock, and J. P. Manning, 2005: Data assimilative hindcast of the Gulf of Maine coastal circulation. *Journal of Geophysical Research-Oceans*, **110**.

- Hermann, A. J., D. B. Haidvogel, E. L. Dobbins, and P. J. Stabeno, 2002: Coupling global and regional circulation models in the coastal Gulf of Alaska. *Progress in Oceanography*, **53**, 335-367.
- Hoteit, I. and B. D. Cornuelle, 2006: Treating Strong Adjoint Sensitivities in Tropical Eddy-Permitting Variational Data Assimilation. *Quarterly Journal of the Royal Meteorological Society*, in press.
- Kleeman, R., A. M. Moore, and N. R. Smith, 1995: Assimilation of Subsurface Thermal Data into a Simple Ocean Model for the Initialization of an Intermediate Tropical Coupled Ocean-Atmosphere Forecast Model. *Monthly Weather Review*, **123**, 3103-3113.
- Klinker, E., F. Rabier, G. Kelly, and J. F. Mahfouf, 2000: The ECMWF operational implementation of four-dimensional variational assimilation. III: Experimental results and diagnostics with operational configuration. *Quarterly Journal of the Royal Meteorological Society*, **126**, 1191-1215.
- Kone, V., E. Machu, P. Penven, V. Andersen, V. Garçon, P. Freon, and H. Demarcq, 2005: Modeling the primary and secondary productions of the southern Benguela upwelling system: A comparative study through two biogeochemical models. *Global Biogeochemical Cycles*, **19**.
- Kosters, F., R. Kase, K. Fleming, and D. Wolf, 2004: Denmark Strait overflow for Last Glacial Maximum to Holocene conditions. *Paleoceanography*, **19**.
- Kurapov, A. L. and E. Di Lorenzo, 2006: Data assimilation test of the tangent linear and adjoint ROMS: shallow water channel flow. *Ocean Modelling*, (this issue).
- Kurapov, A. L., G. D. Egbert, R. N. Miller, and J. S. Allen, 2002: Data assimilation in a baroclinic coastal ocean model: Ensemble statistics and comparison of methods. *Monthly Weather Review*, **130**, 1009-1025.
- Kurapov, A. L., G. D. Egbert, J. S. Allen, R. N. Miller, S. Y. Erofeeva, and P. M. Kosro, 2003: The M-2 internal tide off Oregon: Inferences from data assimilation. *Journal of Physical Oceanography*, **33**, 1733-1757.
- Lea, D. J., T. W. N. Haine, and R. F. Gasparovic, 2006: Irminger Sea circulation using variational data assimilation. *Quarterly Journal of the Royal Meteorological Society*, in press.
- Lermusiaux, P. F. J. and A. R. Robinson, 1999: Data assimilation via error subspace statistical estimation. Part I: Theory and schemes. *Monthly Weather Review*, **127**, 1385-1407.
- Levin, J. C., D. B. Haidvogel, B. Chua, A. F. Bennett, and M. Iskandarani, 2006: Euler-Lagrange equations for the spectral element shallow water system. *Ocean Modelling*, **12**, 348-377.
- Lorenc, A. C., 1997: Development of an operational variational assimilation scheme. *Journal of the Meteorological Society of Japan*, **75**, 339-346.
- , 2003: Modelling of error covariances by 4D-Var data assimilation. *Quarterly Journal of the Royal Meteorological Society*, **129**, 3167-3182.
- Lorenc, A. C., R. S. Bell, and B. Macpherson, 1991: The Meteorological-Office Analysis Correction Data Assimilation Scheme. *Quarterly Journal of the Royal Meteorological Society*, **117**, 59-89.
- Luong, B., J. Blum, and J. Verron, 1998: A variational method for the resolution of a data assimilation problem in oceanography. *Inverse Problems*, **14**, 979-997.
- Lyard, F. H., 1999: Data assimilation in a wave equation: A variational representer approach for the Grenoble tidal model. *Journal of Computational Physics*, **149**, 1-31.
- Lynch, D. R. and C. G. Hannah, 2001: Inverse model for limited-area hindcasts on the continental shelf. *Journal of Atmospheric and Oceanic Technology*, **18**, 962-981.
- Lynch, D. R. and C. E. Naimie, 2002: Hindcasting the Georges Bank circulation, Part II: wind-band inversion. *Continental Shelf Research*, **22**, 2191-2224.
- Lynch, D. R., C. E. Naimie, and C. G. Hannah, 1998: Hindcasting the Georges bank circulation. Part I: Detiding. *Continental Shelf Research*, **18**, 607-639.

- Mahfouf, J. F. and F. Rabier, 2000: The ECMWF operational implementation of four-dimensional variational assimilation. II: Experimental results with improved physics. *Quarterly Journal of the Royal Meteorological Society*, **126**, 1171-1190.
- Malanotte-Rizzoli, P., 1996: *Modern Approach to Data Assimilation in Ocean Modeling*. Vol. 61, *Oceanography Series*, Elsevier, 455 pp.
- Malanotte-Rizzoli, P., K. Hedstrom, H. Arango, and D. B. Haidvogel, 2000: Water mass pathways between the subtropical and tropical ocean in a climatological simulation of the North Atlantic ocean circulation. *Dynamics of Atmospheres and Oceans*, **32**, 331-371.
- Marchesiello, P., J. C. McWilliams, and A. Shchepetkin, 2003: Equilibrium structure and dynamics of the California Current System. *Journal of Physical Oceanography*, **33**, 753-783.
- Marotzke, J., R. Giering, K. Q. Zhang, D. Stammer, C. Hill, and T. Lee, 1999: Construction of the adjoint MIT ocean general circulation model and application to Atlantic heat transport sensitivity. *Journal of Geophysical Research-Oceans*, **104**, 29529-29547.
- Marshall, J., A. Adcroft, C. Hill, L. Perelman, and C. Heisey, 1997: A finite-volume, incompressible Navier Stokes model for studies of the ocean on parallel computers. *Journal of Geophysical Research-Oceans*, **102**, 5753-5766.
- Miller, A. J. and B. D. Cornuelle, 1999: Forecasts from fits of frontal fluctuations. *Dynamics of Atmospheres and Oceans*, **29**, 305-333.
- Miller, A. J., E. Di Lorenzo, D. J. Neilson, B. D. Cornuelle, and J. R. Moisan, 2000: Modeling CalCOFI observations during El Nino: Fitting physics and biology. *California Cooperative Oceanic Fisheries Investigations Reports*, **41**, 87-97.
- Miller, A. J., E. Di Lorenzo, D. J. Neilson, H. J. Kim, A. Capotondi, M. A. Alexander, S. J. Bograd, F. B. Schwing, R. Mendelsohn, K. Hedstrom, and D. L. Musgrave, 2005: Interdecadal changes in mesoscale eddy variance in the Gulf of Alaska circulation: Possible implications for the Steller sea lion ecline. *Atmosphere-Ocean*, **43**, 231-240.
- Miller, R. N., E. F. Carter, and S. T. Blue, 1999: Data assimilation into nonlinear stochastic models. *Tellus Series a-Dynamic Meteorology and Oceanography*, **51**, 167-194.
- Mooers, C. N. K., 1999: *Coastal Ocean Prediction*. Vol. 56, *Estuarine Series*, American Geophysical Union, 523 pp.
- Moore, A. M., 1991: Data Assimilation in a Quasi-Geostrophic Open-Ocean Model of the Gulf-Stream Region Using the Adjoint Method. *Journal of Physical Oceanography*, **21**, 398-427.
- Moore, A. M., H. G. Arango, E. Di Lorenzo, B. D. Cornuelle, A. J. Miller, and D. J. Neilson, 2004: A comprehensive ocean prediction and analysis system based on the tangent linear and adjoint of a regional ocean model. *Ocean Modelling*, **7**, 227-258.
- Morrow, R. and P. DeMey, 1995: Adjoint assimilation of altimetric, surface drifter, and hydrographic data in a quasi-geostrophic model of the Azores Current. *Journal of Geophysical Research-Oceans*, **100**, 25007-25025.
- Ngodock, H. E., 2005: Efficient implementation of covariance multiplication for data assimilation with the representer method. *Ocean Modelling*, **8**, 237-251.
- Ngodock, H. E., B. S. Chua, and A. E. Bennett, 2000: Generalized inverse of a reduced gravity primitive equation ocean model and Tropical Atmosphere-Ocean data. *Monthly Weather Review*, **128**, 1757-1777.
- Parrish, D. F., J. C. Derber, R. J. Purser, W. S. Wu, and Z. X. Pu, 1997: The NCEP global analysis system: Recent improvements and future plans. *Journal of the Meteorological Society of Japan*, **75**, 359-365.
- Penven, P., V. Echevin, J. Pasapera, F. Colas, and J. Tam, 2005: Average circulation, seasonal cycle, and mesoscale dynamics of the Peru Current System: A modeling approach. *Journal of Geophysical Research-Oceans*, **110**.
- Pinardi, N., I. Allen, E. Demirov, P. De Mey, G. Korres, A. Lascaratos, P. Y. Le Traon, C. Maillard, G. Manzella, and C. Tziavos, 2003: The Mediterranean ocean forecasting system: first phase of implementation (1998-2001). *Annales Geophysicae*, **21**, 3-20.

- Rabier, F. and P. Courtier, 1992: 4-Dimensional Assimilation in the Presence of Baroclinic Instability. *Quarterly Journal of the Royal Meteorological Society*, **118**, 649-672.
- Ricci, S., A. T. Weaver, J. Vialard, and P. Rogel, 2005: Incorporating state-dependent temperature-salinity constraints in the background error covariance of variational ocean data assimilation. *Monthly Weather Review*, **133**, 317-338.
- Robertson, R., A. Beckmann, and H. Hellmer, 2003: M-2 tidal dynamics in the Ross Sea. *Antarctic Science*, **15**, 41-46.
- Robinson, A. R., 1999: Forecasting and simulating coastal ocean processes and variabilities with the Harvard Ocean Prediction System, in Coastal Ocean Prediction. *Coastal Estuarine Studies* M. C. N. K., Ed., AGU, 77-100.
- Robinson, A. R. and L. J. Walstad, 1987: The Harvard Open Ocean Model - Calibration and Application to Dynamic Process, Forecasting, and Data Assimilation Studies. *Applied Numerical Mathematics*, **3**, 89-131.
- Rosmond, T. and L. Xu, 2006: Development of NAVDAS-AR: non-linear formulation and outer loop tests. *Tellus Series a-Dynamic Meteorology and Oceanography*, **58**, 45-58.
- Schroter, J., U. Seiler, and M. Wenzel, 1993: Variational Assimilation of Geosat Data into an Eddy-Resolving Model of the Gulf-Stream Extension Area. *Journal of Physical Oceanography*, **23**, 925-953.
- Scott, R. K., J. S. Allen, G. D. Egbert, and R. N. Miller, 2000: Assimilation of surface current measurements in a coastal ocean model. *Journal of Physical Oceanography*, **30**, 2359-2378.
- Seiler, U., 1993: Estimation of Open Boundary-Conditions with the Adjoint Method. *Journal of Geophysical Research-Oceans*, **98**, 22855-22870.
- Shchepetkin, A. F. and J. C. McWilliams, 2005: The regional oceanic modeling system (ROMS): a split-explicit, free-surface, topography-following-coordinate oceanic model. *Ocean Modelling*, **9**, 347-404.
- She, J. and J. M. Klinck, 2000: Flow near submarine canyons driven by constant winds. *Journal of Geophysical Research-Oceans*, **105**, 28671-28694.
- Smedstad, O. M., H. E. Hurlburt, E. J. Metzger, R. C. Rhodes, J. F. Shriver, A. J. Wallcraft, and A. B. Kara, 2003: An operational Eddy resolving 1/16 degrees global ocean nowcast/forecast system. *Journal of Marine Systems*, **40**, 341-361.
- Stammer, D., K. Ueyoshi, A. Kohl, W. G. Large, S. A. Josey, and C. Wunsch, 2004: Estimating air-sea fluxes of heat, freshwater, and momentum through global ocean data assimilation. *Journal of Geophysical Research-Oceans*, **109**.
- Stammer, D., C. Wunsch, R. Giering, C. Eckert, P. Heimbach, J. Marotzke, A. Adcroft, C. N. Hill, and J. Marshall, 2003: Volume, heat, and freshwater transports of the global ocean circulation 1993-2000, estimated from a general circulation model constrained by World Ocean Circulation Experiment (WOCE) data. *Journal of Geophysical Research-Oceans*, **108**.
- Taillandier, V., V. Echevin, L. Mortier, and J. L. Devenon, 2004: Controlling boundary conditions with a four-dimensional variational data-assimilation method in a non-stratified open coastal model. *Ocean Dynamics*, **54**, 284-298.
- Talagrand, O. and P. Courtier, 1987: Variational Assimilation of Meteorological Observations with the Adjoint Vorticity Equation .1. Theory. *Quarterly Journal of the Royal Meteorological Society*, **113**, 1311-1328.
- Thepaut, J. N. and P. Courtier, 1991: 4-Dimensional Variational Data Assimilation Using the Adjoint of a Multilevel Primitive-Equation Model. *Quarterly Journal of the Royal Meteorological Society*, **117**, 1225-1254.
- Tziperman, E., W. C. Thacker, R. B. Long, and S. M. Hwang, 1992: Oceanic Data-Analysis Using a General-Circulation Model .1. Simulations. *Journal of Physical Oceanography*, **22**, 1434-1457.
- Tziperman, E., W. C. Thacker, R. B. Long, S. M. Hwang, and S. R. Rintoul, 1992: Oceanic Data-Analysis Using a General-Circulation Model .2. a North-Atlantic Model. *Journal of Physical Oceanography*, **22**, 1458-1485.

- Uboldi, F. and M. Kamachi, 2000: Time-space weak-constraint data assimilation for nonlinear models. *Tellus Series a-Dynamic Meteorology and Oceanography*, **52**, 412-421.
- Vialard, J., A. T. Weaver, D. L. T. Anderson, and P. Delecluse, 2003: Three- and four-dimensional variational assimilation with a general circulation model of the tropical Pacific Ocean. Part II: Physical validation. *Monthly Weather Review*, **131**, 1379-1395.
- Warner, J. C., W. R. Geyer, and J. A. Lerczak, 2005: Numerical modeling of an estuary: A comprehensive skill assessment. *Journal of Geophysical Research-Oceans*, **110**.
- Weaver, A. and P. Courtier, 2001: Correlation modelling on the sphere using a generalized diffusion equation. *Quarterly Journal of the Royal Meteorological Society*, **127**, 1815-1846.
- Weaver, A. T., J. Vialard, and D. L. T. Anderson, 2003: Three- and four-dimensional variational assimilation with a general circulation model of the tropical Pacific Ocean. Part I: Formulation, internal diagnostics, and consistency checks. *Monthly Weather Review*, **131**, 1360-1378.
- Wilkin, J. L., H. G. Arango, D. B. Haidvogel, C. S. Lichtenwalner, S. M. Glenn, and K. S. Hedstrom, 2005: A regional ocean modeling system for the Long-term Ecosystem Observatory. *Journal of Geophysical Research-Oceans*, **110**.
- Wunsch, C., 1996: *The Ocean Circulation Inverse Problem*. Cambridge University Press, 422 pp.
- Zou, X., H. Liu, J. Derber, J. G. Sela, R. Treadon, I. M. Navon, and B. Wang, 2001: Four-dimensional variational data assimilation with a diabatic version of the NCEP global spectral model: System development and preliminary results. *Quarterly Journal of the Royal Meteorological Society*, **127**, 1095-1122.
- Zupanski, M., D. Zupanski, T. Vukicevic, K. Eis, and T. I. V. Haar, 2005: CIRA/CSU four-dimensional variational data assimilation system. *Monthly Weather Review*, **133**, 829-843.

Figure captions

Figure 1: Panel (A) model grid and bathymetry. The model has closed boundaries in the east and west and periodic open boundary conditions in the south and north. The black (x) indicate the sampling network used in the assimilation experiments. Panel (B) vertical cross-shore sections of temperature and the velocity components. The black (x) show the location of the vertical sampling grid. The fields show the typical baroclinic structure in January.

Figure 2: The representer functions for two cross-shore velocity observations on DAY=6 located at the black (x). These functions are the space-time cross-covariances between the observations and the entire model temperature and velocity fields. Here we show only the surface component. The first column shows the spatial structure of the covariances for the same day as the observations (DAY=6), while the second column (DAY=10) shows also the temporal structure at future time. Note the strong stirring action of the flow field on the structure of the covariances. The symbols U,V,T denote cross-shore and alongshore velocity anomalies, and temperature anomalies.

Figure 3: Maps of upper ocean temperature (0-100 m) for hindcast period from DAY=0 (initial condition) to DAY=10 (end of assimilation window). The first column represent the “true” state,

the second column is the basic state integration initialized from climatology, the third column is the result from the weak constraint assimilation experiment (Exp'weakH) and the fourth column is the result from the strong constraint assimilation experiment (Exp'strongH).

Figure 4: Dimensional misfits between synthetic observations and model before and after the assimilation. Black line is misfit between observations and first model guess. Gray line is misfit between synthetic observations and model solution after assimilation. The upper two rows show the results for the WEAK (Exp'weakH) and STRONG (Exp'strongH) constraint case using the HIRES sampling array to collect observations. The lower two rows show results for WEAK (Exp'weakC) and STRONG (Exp'strongC) constraint case using the COARSE sampling array. The first column is temperature differences, second column cross-shore velocity and third column alongshore velocity.

Figure 5: Hindcast and forecast skill scores for upper ocean temperature (0-100 m) and alongshore velocity. Skill is defined based on the RMS difference from the truth (see section 5.6 in text). A perfect skill value is 1. The red line is the skill of the weak constraint solution and the green line of the strong constraint. The blue line corresponds to the skill of persistence. The field used to compute the persistence skill is computed by taking the available observations and performing an objective mapping to interpolate at the location where observations are not available. In the forecast window (DAY 10-30) no observations are used to constrain the model trajectory. The upper row shows result using the HIRES sampling array and the lower row the COARSE array.

Figure 6: Maps of upper ocean temperature (0-100 m) in the forecast window from DAY=14 (4 days after the end of the assimilation window) to DAY=26. The first column represent the "true" state, the second column is the basic state integration initialized with climatology, the third column is the result from the weak constraint assimilation experiment (Exp'weakC) and the fourth column is the result from the strong constraint assimilation experiment (Exp'strongC). The forecast are performed using the nonlinear model initialized with the solutions of the assimilation experiments at DAY=10.

Figure 7: Skill for upper ocean temperature (0-100 m) in the assimilation window. The gray line is the skill of the weak constraint solution for the HIRES case (as in Fig. 5). The zero skill line (thick black) is climatology. The black continuous line with dots is the skill of the linearized model (REP-roms) initialized with the true initial condition and integrated forward using climatology as the basic state for the linearization. The continuous black line is same as the

continuous line with dots except that the basic state for the linearization is the “true” solution. In theory the REP-roms should converge to the true state by iterating and updating the basic state, however this is not the case. The skill of the weak constraint solution performs better implying that the REP-roms state will never converge to the true nonlinear state for the upwelling test case (see section 5.7). This lack of convergence is associated with linear instabilities in the RP-ROMS.

Tables

Experiment Name	STRONG Constraint	WEAK Constraint	Observation Sampling
Exp_weakH		YES	HIRES
Exp_strongH	YES		HIRES
Exp_weakC		YES	COARSE
Exp_strongC	YES		COARSE

Table 1: Assimilation experiments using the weak and strong constraint approach.

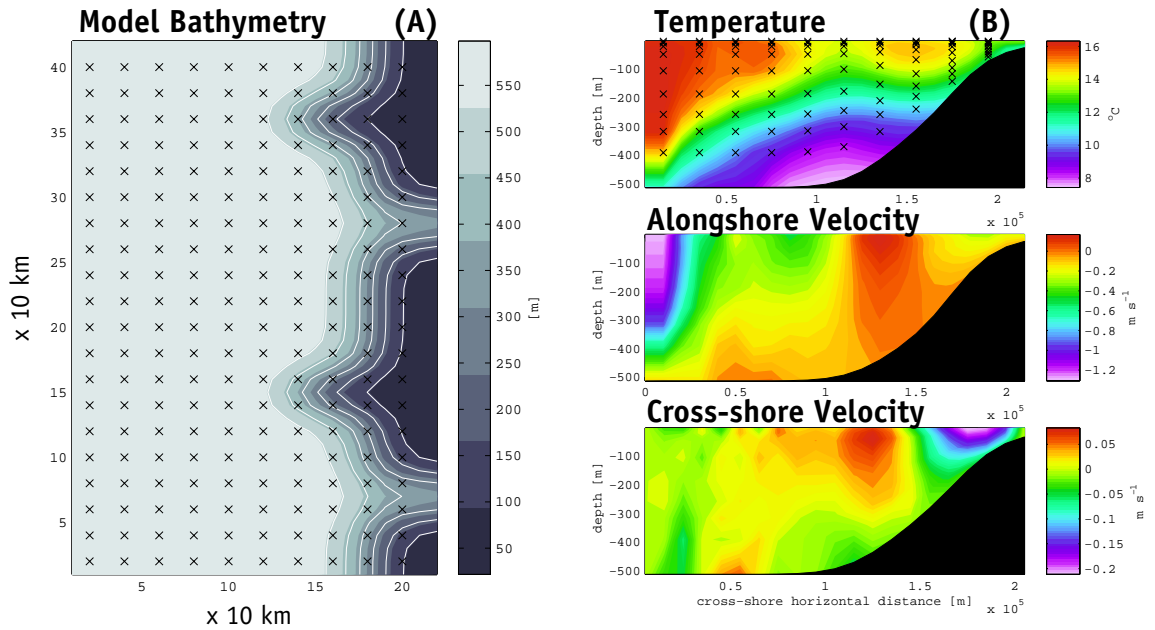


Figure 1: Panel (A) model grid and bathymetry. The model has closed boundaries in the east and west and periodic open boundary conditions in the south and north. The black (x) indicate the sampling network used in the assimilation experiments. Panel (B) vertical cross-shore sections of temperature and the velocity components. The black (x) show the location of the vertical sampling grid. The fields show the typical baroclinic structure in January.

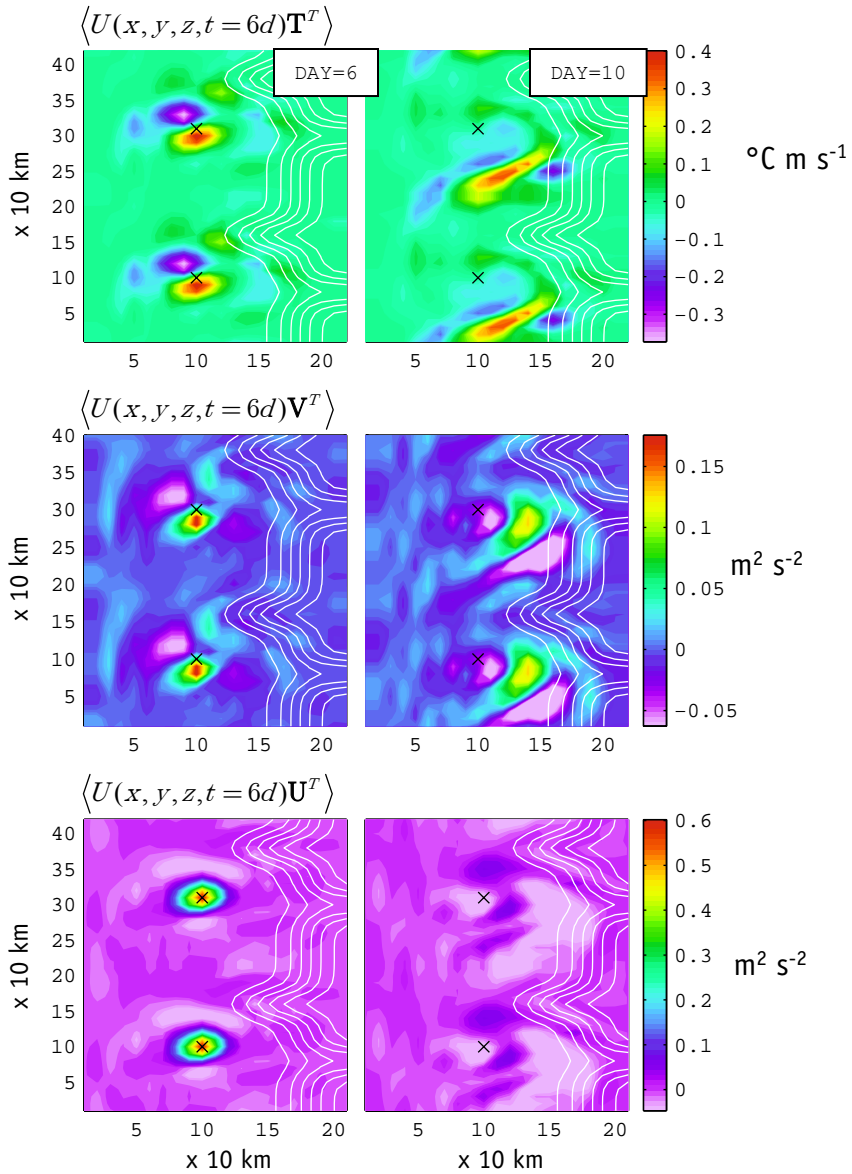


Figure 2: The representer functions for two cross-shore velocity observations on DAY=6 located at the black (x). These functions are the space-time cross-covariances between the observations and the entire model temperature and velocity fields. Here we show only the surface component. The first column shows the spatial structure of the covariances for the same day as the observations (DAY=6), while the second column (DAY=10) shows also the temporal structure at future time. Note the strong stirring action of the flow field on the structure of the covariances. The symbols U,V,T denote cross-shore and alongshore velocity anomalies, and temperature anomalies.

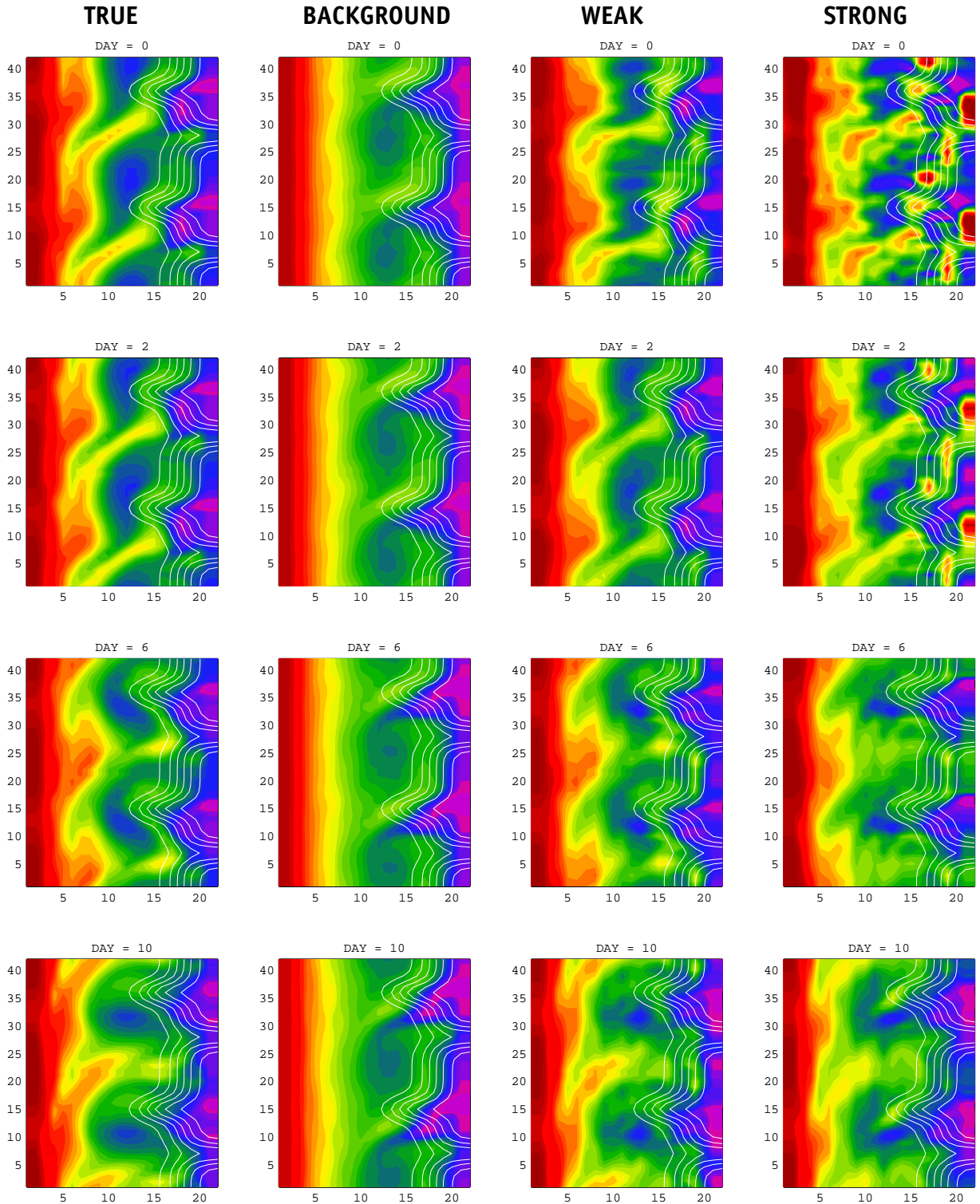


Figure 3: Maps of upper ocean temperature (0-100 m) for hindcast period from DAY=0 (initial condition) to DAY=10 (end of assimilation window). The first column represent the “true” state, the second column is the background integration initialized from climatology, the third column is the result from the weak constraint assimilation experiment (Exp’weakH) and the fourth column is the result from the strong constraint assimilation experiment (Exp’strongH)

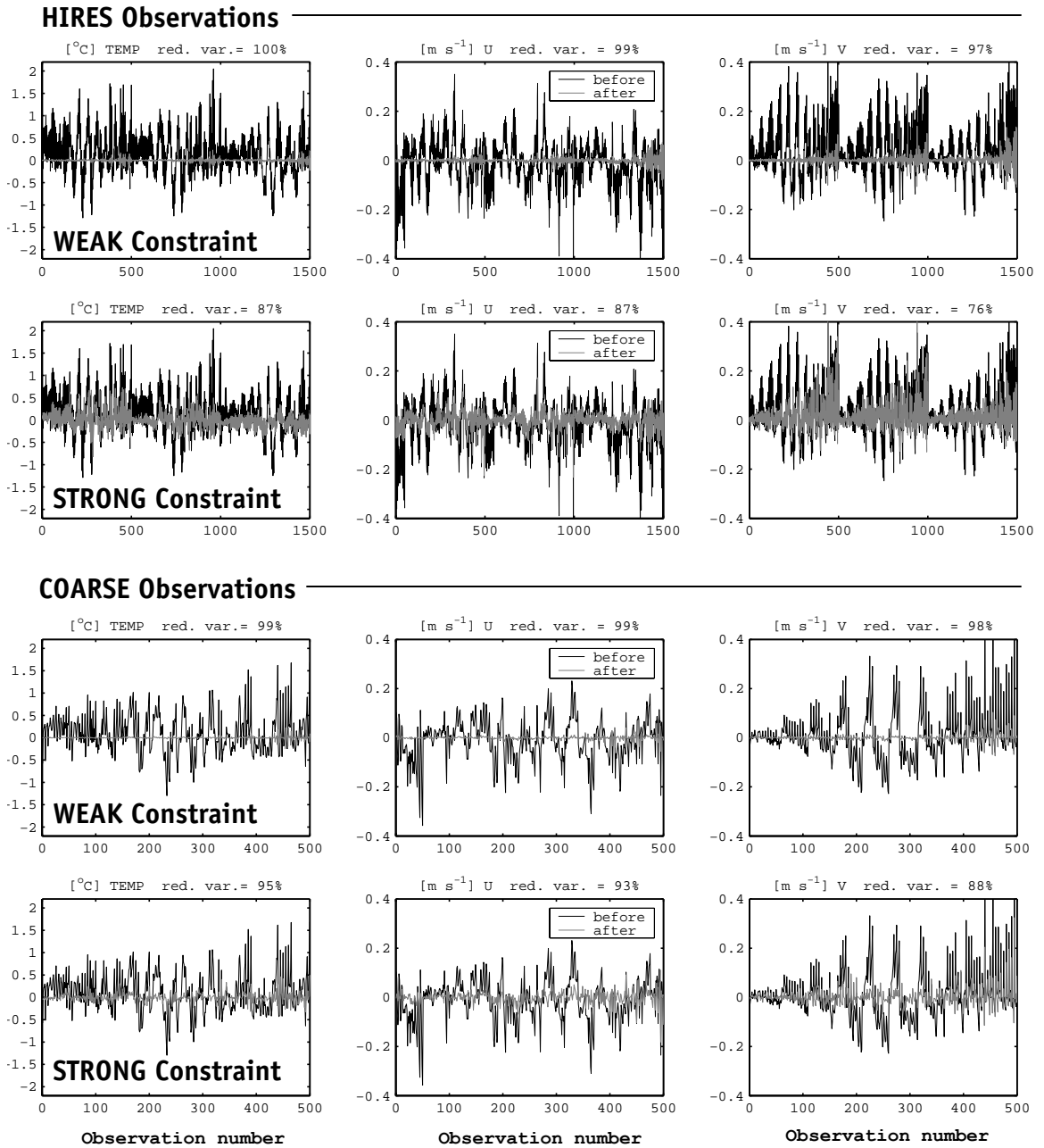


Figure 4: Dimensional misfits between synthetic observations and model before and after the assimilation. Black line is misfit between observations and first model guess. Gray line is misfit between synthetic observations and model solution after assimilation. The upper two rows show the results for the WEAK (Exp'weakH) and STRONG (Exp'strongH) constraint case using the HIRES sampling array to collect observations. The lower two rows show results for WEAK (Exp'weakC) and STRONG (Exp'strongC) constraint case using the COARSE sampling array. The first column is temperature differences, second column cross-shore velocity and third column alongshore velocity.

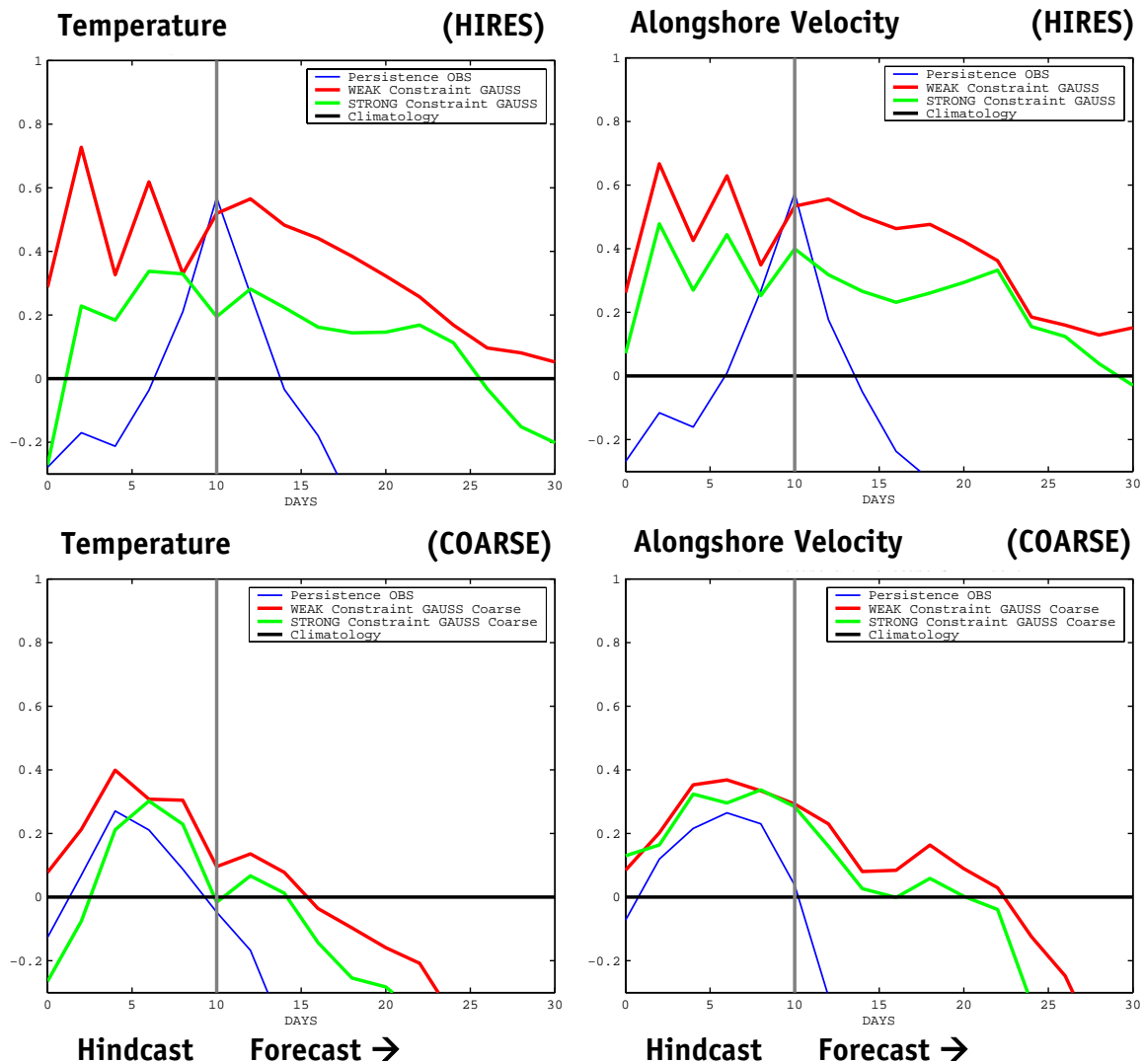


Figure 5: Hindcast and forecast skill scores for upper ocean temperature (0-100 m) and alongshore velocity. Skill is defined based on the RMS difference from the truth (see section 5.6 in text). A perfect skill value is 1. The red line is the skill of the weak constraint solution and the green line of the strong constraint. The blue line corresponds to the skill of persistence. The field used to compute the persistence skill is computed by taking the available observations and performing an objective mapping to interpolate at the location where observations are not available. In the forecast window (DAY 10-30) no observations are used to constrain the model trajectory. The upper row shows result using the HIRES sampling array and the lower row the COARSE array.

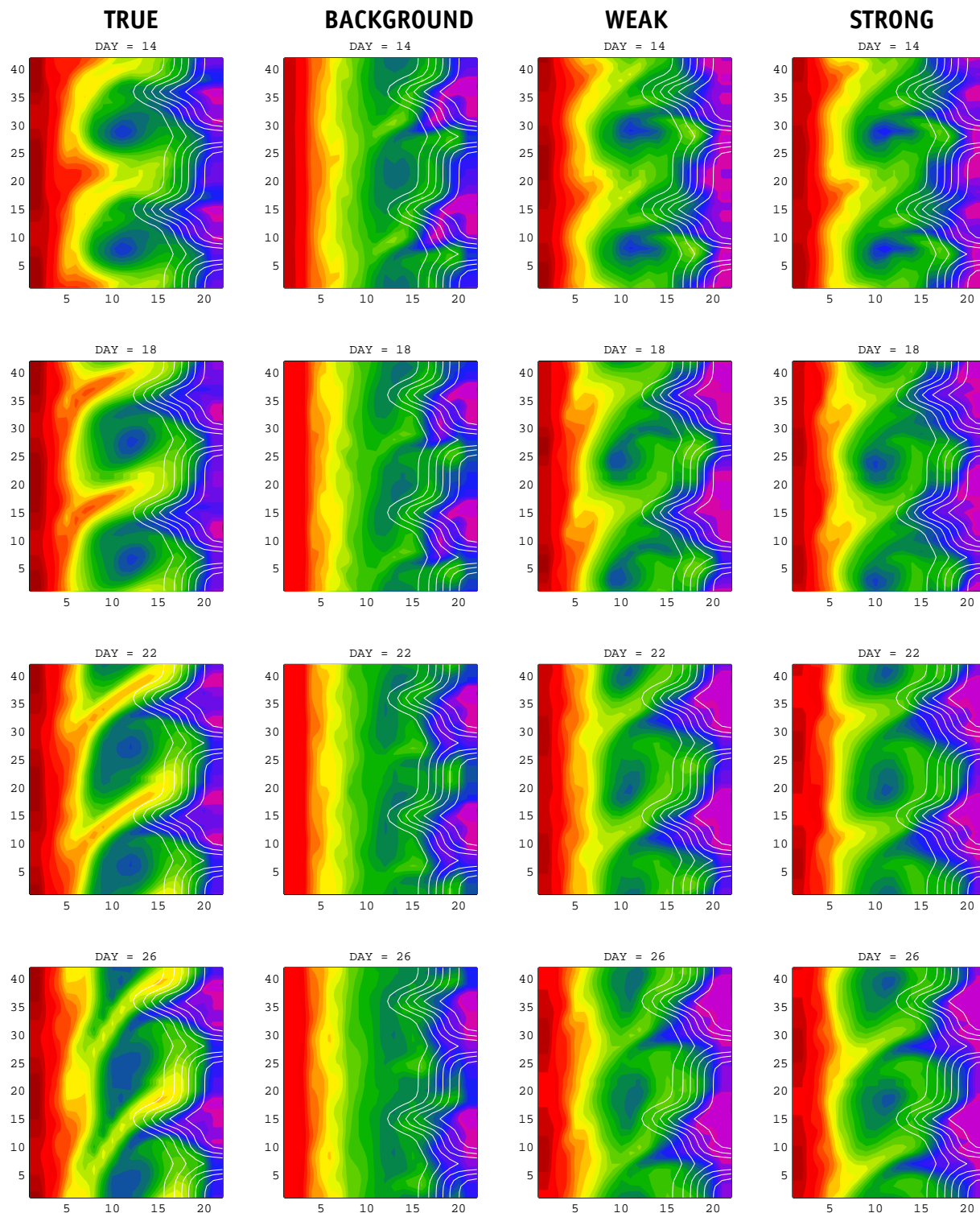


Figure 6: Maps of upper ocean temperature (0-100 m) in the forecast window from DAY=14 (4 days after the end of the assimilation window) to DAY=26. The first column represent the “true” state, the second column is the background integration initialized with climatology, the third column is the result from the weak constraint assimilation experiment (Exp’weakC) and the fourth column is the result from the strong constraint assimilation experiment (Exp’strongC). The forecast are performed using the nonlinear model initialized with the solutions of the assimilation experiments at DAY=10.

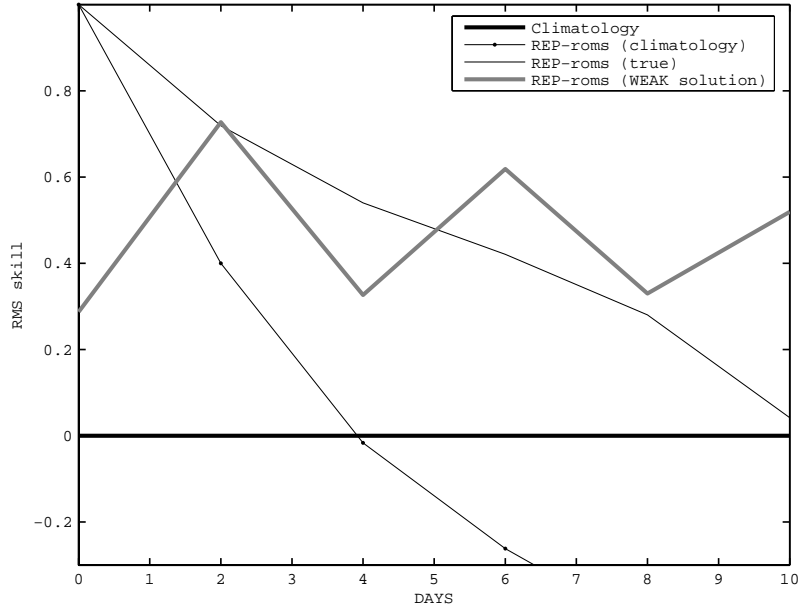


Figure 7: Skill for upper ocean temperature (0-100 m) in the assimilation window. The gray line is the skill of the weak constraint solution for the HIRES case (as in Fig. 5). The zero skill line (thick black) is climatology. The black continuous line with dots is the skill of the linearized model (REP-roms) initialized with the true initial condition and integrated forward using climatology as the background state for the linearization. The continuous black line is same as the continuous line with dots except that the background state for the linearization is the “true” solution. In theory the REP-roms should converge to the true state by iterating and updating the background state, however this is not the case. The skill of the weak constraint solution performs better implying that the REP-roms state will never converge to the true nonlinear state for the upwelling test case (see section 5.7). This lack of convergence is associated with linear instabilities in the RP-ROMS.